Impact of the rippling of a perpendicular shock front on ion dynamics

Z. W. Yang, Bertrand Lembège, Q. M. Lu

Impact of the rippling of a perpendicular shock front on ion dynamics

Z. W. Yang,[1,2] B. Lembège,[2] and Q. M. Lu[3]

Received 2 October 2011; revised 10 May 2012; accepted 3 June 2012; published 27 July 2012.

[1] Both hybrid/full particle simulations and recent experimental results have clearly evidenced that the front of a supercritical quasi-perpendicular shock can be rippled. Recent two-dimensional simulations have focused on two different types of shock front rippling: (1) one characterized by a small spatial scale along the front is supported by lower hybrid wave activity, (2) the other characterized by a large spatial scale along the front is supported by the emission of large amplitude nonlinear whistler waves. These two rippled shock fronts are self-consistently observed when the static magnetic field is perpendicular to (so called "B_0-OUT" case) or within (so called "B_0-IN" case) the simulation plane, respectively. On the other hand, several studies have been made on the reflection and energization of incoming ions with a shock but most have been restricted to a one dimensional shock profile only (no rippling effects). Herein, two-dimensional test particle simulations based on strictly perpendicular shock profiles chosen at a fixed time in two-dimensional Particle-in-cell (PIC) simulations, are performed in order to investigate the impact of the shock front ripples on incident ion (H^+) dynamics. The acceleration mechanisms and energy spectra of the test-ions (described by shell distributions with different initial kinetic energy) interacting with a rippled shock front are analyzed in detail. Both "B_0-OUT" and "B_0-IN" cases are considered separately; in each case, y-averaged (front rippling excluded) and non-averaged (front rippling included) profiles will be analyzed. Present results show that: (1) the incident ions suffer both shock drift acceleration (SDA) and shock surfing acceleration (SSA) mechanisms. Moreover, a striking feature is that SSA ions not only are identified at the ramp but also within the foot which confirms previous 1-D simulation results; (2) the percentage of SSA ions increases with initial kinetic energy, a feature which persists well with a rippled shock front; (3) furthermore, the ripples increase the porosity of the shock front, and more directly transmitted (DT) ions are produced; these strongly affect the relative percentage of the different identified classes of ions (SSA, SDA and DT ions), their average kinetic energy and their relative contribution to the resulting downstream energy spectra; (4) one key impact of the ripples is a strong diffusion of ions (in particular through the frontiers of their injection angle domains and in phase space which are blurred out) which leads to a mixing of the different ion classes. This diffusion increases with the size of the spatial scale of the front ripples; (5) through this diffusion, an ion belonging to a given category (SSA, SDA, or DT) in y-averaged case changes class in non-averaged case without one-to-one correspondence.

Citation: Yang, Z. W., B. Lembège, and Q. M. Lu (2012), Impact of the rippling of a perpendicular shock front on ion dynamics, *J. Geophys. Res.*, *117*, A07222, doi:10.1029/2011JA017211.

1. Introduction

[2] Collisionless shocks are of strong interest in space physics, plasma physics and astrophysics. They are commonly believed to be important sources of high-energy particles, such as Solar Energetic Particles (SEPs) [*Reames*, 2000; *Zank et al.*, 2006; *Mikić and Lee*, 2006], Anomalous Cosmic Rays (ACRs) [*Ellison et al.*, 1999; *Czechowski et al.*, 2001; *Giacalone and Decker*, 2010] and Galactic Cosmic Rays (GCRs) [*Ellison and Reynolds*, 1991; *Meyer et al.*, 1998; *Berezhko and Völk*, 2000]. In situ measurements of the terrestrial bow shock made by CLUSTER mission

[1]SOA Key Laboratory for Polar Science, Polar Research Institute of China, Shanghai, China.
[2]LATMOS-UVSQ-IPSL-CNRS, Guyancourt, France.
[3]CAS Key Laboratory of Basic Plasma Physics, School of Earth and Space Sciences, University of Science and Technology of China, Hefei, China.

Corresponding author: B. Lembège, LATMOS-UVSQ-IPSL-CNRS, Guyancourt FR-78280, France. (bertrand.lembege@latmos.ipsl.fr)

0148-0227/12/2011JA017211

[*Walker and Balikhin*, 1999; *Moullard et al.*, 2006; *Mazelle et al.*, 2010], plasma laboratory experiments [*Morse et al.*, 1972], and numerical simulations [*Biskamp and Welter*, 1972; *Forslund et al.*, 1984; *Lembège and Dawson*, 1987; *Winske and Quest*, 1988; *Lembège and Savoini*, 1992; *Nishimura et al.*, 2003; *Scholer and Matsukiyo*, 2004; *Chapman et al.*, 2005] revealed that quasi-perpendicular shocks can be strongly nonstationary in a supercritical regime. Hybrid and Particle-in-cell (PIC) simulations have shown that shock front nonstationarity can result from at least two classes of processes: one class corresponds to processes developing mainly along the shock normal. One robust process is the so called shock front self-reformation due to the accumulation of reflected ions which develops over a foot distance from the ramp [*Biskamp and Welter*, 1972; *Lembège and Dawson*, 1987; *Lembège and Savoini*, 1992; *Hada et al.*, 2003; *Scholer et al.*, 2003]. The other class corresponds to processes developing along the shock front and are responsible for the shock front rippling. There are at least three types of ripples: (1) short scale (below ion inertial length) lower-hybrid waves (typically about perpendicular to the magnetic field) supported by cross field currents instabilities [*Lembège and Savoini*, 1992], (2) longer scale (of the order of one or a few ion inertial lengths) oblique whistler waves [*Hellinger et al.*, 2007; *Lembège et al.*, 2009], and (3) even much longer "Alfvén wave" ripples (several ion inertial lengths) [*Winske and Quest*, 1988; *Saito and Umeda*, 2011]. *Lowe and Burgess* [2003] investigated these Alfvén ripples [*Winske and Quest*, 1988] and interpreted them as surface waves but did not exclude the possibility that these ripples are generated by the proton temperature anisotropy as originally proposed by *Winske and Quest* [1988].

[3] Diffusive shock acceleration (DSA) [*Axford et al.*, 1977; *Bell*, 1978a, 1978b; *Krymsky*, 1977; *Blandford and Ostriker*, 1978; *Lee*, 1983; *Blandford and Eichler*, 1987; *Webb et al.*, 1995] is the most widely accepted theory for particle acceleration for quasi-parallel shocks. However, a similar theory does not work efficiently at low energies at quasi-perpendicular shocks, where the reflected ions return to the shocks almost immediately due to their gyromotion in the upstream magnetic field. Therefore, shock drift acceleration (SDA) [*Hudson*, 1965; *Webb et al.*, 1983; *Decker and Vlahos*, 1985; *Decker*, 1988; *Begelman and Kirk*, 1990; *Chalov*, 2001] and shock surfing acceleration (SSA) [*Sagdeev*, 1966; *Katsouleas and Dawson*, 1983; *Zank et al.*, 1996; *Lee et al.*, 1996; *Lee*, 1999; *Shapiro and Üçer*, 2003] are considered to play important roles in ion acceleration or pre-acceleration at quasi-perpendicular shocks. However, the problem is that comprehensive and detailed analysis of SSA/SDA mechanisms for rippled shock front, where the front rippling is included self-consistently, has not been performed yet.

[4] *Decker* [1990] considered the acceleration of ions within a rippled shock front by using a quasi-static surface corrugation described phenomenologically by sinusoidal function. The front ripples are characterized by an amplitude A and a spatial scale L that is large compared to an energetic ion's gyroradius r_g, i.e., $r_g \ll L$. The authors found that a few injected ions are trapped by the ripples, undergo many reflections within the front and are accelerated nonadiabatically. But, this work is based on a stationary shock front along the shock normal, and the used front rippling is not consistent. Recently, *Yang et al.* [2009a] investigated the ion acceleration by using test particle simulations based on nonstationary shock profiles (along the shock normal) issued from self-consistent 1-D PIC simulations of supercritical perpendicular reforming shocks. They focused on the impact of shock front self-reformation on ion acceleration, and found that SDA and SSA mechanisms compete with each other.

[5] Recent works [*Hellinger et al.*, 2007; *Lembège et al.*, 2009] based on 2-D PIC and 2-D hybrid simulations of a strictly perpendicular shock have examined two competitive mechanisms of nonstationarity: the shock front self-reformation (mainly along the shock normal) and the shock front nonstationary triggered by an emission of large amplitude whistler waves which are at the origin of an important shock front rippling. This competition is based on the different configurations of the upstream magnetic field: (1) when the upstream ambient magnetic field B_0 lies outside the simulation plane (so called "B_0-OUT"), the self-reformation along the shock normal is dominant, and the shock front rippling is only characterized by a relatively small spatial scale (less than 1 c/ω_{pi} where c/ω_{pi} is the ion inertial length). The amplitude of this rippling is too weak to diffuse noticeably the reflected ions (which maintain some coherent motion during their gyromotion) and does not impede the self-reformation which clearly persists and is the dominant nonstationary process; (2) in contrast, when the upstream ambient magnetic field B_0 lies within the simulation plane, large amplitude whistler waves are emitted within the front and are at the origin of a large spatial scale rippling (several c/ω_{pi} along the front). These waves largely interact with reflected ions which become diffuse and cannot feed any more the front self-reformation which disappears. However, at present, one still ignores the impact of different scales of the shock front rippling on SSA and SDA mechanisms, and on their respective energy spectra.

[6] *Yang et al.* [2009a] have separated the incoming test particle ions into reflected and directly transmitted ions during their interaction with the front of a supercritical perpendicular shock (similarly as in *Burgess et al.* [1989]), and then have investigated the mechanisms of ion acceleration. Most energetic particles correspond to the reflected ions which are accelerated by SSA and SDA mechanisms. The ion dynamics depends largely on the structures of the shock with which incoming ions interact. Therefore as the shock evolves with time, the nonstationarity effects cannot be neglected. In extension to the previous results obtained at stationary perpendicular shocks by using hybrid simulations [*Burgess et al.*, 1989], *Yang et al.* [2009a] found that (1) whether a given ion is accelerated primarily depends on the time at which ions interact with the shock, and (2) energetic particles (SSA and SDA ions) come from a limited portion of the incident velocity distribution, rather than being randomly selected. However, in the hybrid simulations of *Burgess et al.* [1989] where the structure of the shock profile is fixed, none of the reflected ions comes from the core of Maxwellian distribution. In contrast, results of PIC simulations [*Lee et al.*, 2005; *Yang et al.*, 2009a], where the shock front is nonstationary (self-reformation), clearly evidenced the reflected ions come from not only the wings but also the core of the Maxwellian distribution. The wings and the core of the Maxwellian distribution can be considered as a weighted superposition of individual shell velocity distributions with large and small

Table 1. Upstream Plasma Parameters Defined for the 2-D PIC Simulation

	Symbol	Electrons	Ions
Thermal velocity	$\tilde{V}_{thx,y,z}$	0.3	0.012
Debye length	λ_D	0.42	0.34
Larmor gyro radius	$\tilde{\rho}_c$	0.84	13.6
Inertia length	$\tilde{c}/\tilde{\omega}_p$	3.0	60
Gyro frequency	$\tilde{\Omega}_c$	0.5	0.0012
Plasma frequency	$\tilde{\omega}_p$	1.0	0.05
Gyro period	$\tilde{\tau}_c$	13	5027
Plasma beta	β	0.16	0.101

radii, respectively. Thus, the nonstationary shock helps the acceleration of reflected ions with low initial energies (solar wind ions from the core of the Maxwellian distribution or the pickup ions from shell distribution with small radius) rather than the stationary shock.

[7] The present paper represents an extension of a previous work based on 1-D simulations [*Yang et al.*, 2009a, 2009b] to 2-D shock profiles. Herein, we use similar test particle calculations based on fields of shock profiles issued from two-dimensional PIC simulation (where rippling effects are self-consistently included) in order to address the following questions: (1) What is the impact of the shock front rippling on ion acceleration mechanisms and energy spectra? (2) How does this impact differ when considering small and large spatial scale ripples? (3) SSA mechanisms is often invoked as pre-accelerating process taking place before DSA process applies. In which conditions (in terms of particle injection angle and initial kinetic energy), SSA ions can be identified in the presence of front rippling?, and at least (4) how SSA and SDA processes compete with each other in terms of respective occurrence, percentage of ion populations and corresponding efficiency in the energy gain? This paper is organized as follows. In section 2, we briefly describe the numerical model used herein. Section 3 presents the simulation results for small and large scale rippling cases respectively. The main conclusions will be summarized in section 4.

2. Simulation Conditions

[8] Investigating ion acceleration at a rippled shock requires a spatial range large enough for particles to do gyromotion before and after the shock, and a spatial resolution high enough to include the detailed physics for shock front microstructure. We implement a combination of a 2-D PIC simulation to model the shock front fields and of test particle simulations to analyze the dynamics of a large number of energetic ions. First, two-dimensional PIC simulations (where both ions and electrons are treated as individual macroparticles) are performed similar to those of previous work [*Lembège and Savoini*, 1992; *Lembège et al.*, 2009], where the perpendicular planar shock ($\theta_{Bn} = 90°$) is initiated by a magnetic piston (applied current pulse). Therefore, the shock geometry is always defined in the upstream frame: the shock propagates along the x direction. Periodic conditions are used along the direction of the planar shock front (y-axis).

[9] Two 2-D PIC different runs have been initially performed. One where the upstream ambient magnetic field B_0 is perpendicular to the simulation plane which is named B_0-OUT case, and the other where B_0 is lying within the simulation plane (x, y) which is named B_0-IN case. All dimensionless quantities are indicated by a tilde "$\sim$" and are normalized as follows. The spatial coordinate is $\tilde{x} = x/\Delta$; velocity $\tilde{v} = v/\omega_{pe}\Delta$; time $\tilde{t} = \omega_{pe}t$, electric field $\tilde{E} = eE/m_e\omega_{pe}^2\Delta$; magnetic field $\tilde{B} = eB/m_e\omega_{pe}^2\Delta$. The parameters Δ, ω_{pe}, m_e and e are, respectively, the numerical grid size, the electron plasma frequency, the electron mass and the electric charge. These definitions are identical to those used in previous 1-D PIC [*Lembège and Dawson*, 1987], and 2-D PIC simulations [*Lembège and Savoini*, 1992]. The plasma conditions and shock regime used herein are similar to those used in *Lembège et al.* [2009]. All basic parameters are summarized as follows: the plasma simulation box has 6144 × 256 grids with a spatial resolution $\Delta = \Delta x = \Delta y = 1/60(\tilde{c}/\tilde{\omega}_{pi}) = 1/3(\tilde{c}/\tilde{\omega}_{pe})$ (where $\tilde{c}/\tilde{\omega}_{pi}$ and $\tilde{c}/\tilde{\omega}_{pe}$ are the ion and electron inertial lengths respectively), which is high enough to involve all microstructures of the shock front. Initially, the number of particles per cell is 4 for each specie. Velocity of light $\tilde{c} = 3$, and mass ratio of proton and electron $m_i/m_e = 400$. In order to achieve reasonable run times and simulation domains, a ratio of $\omega_{pe}/\Omega_{ce} = 2$ had been used as in *Hada et al.* [2003] and *Matsukiyo et al.* [2007]. The electron/ion temperature ratio is $T_e/T_i = 1.58$; upstream ions and electrons are isotropic so that $\tilde{v}_{thi} = \tilde{v}_{thi,x,y,z}$ and $\tilde{v}_{the} = \tilde{v}_{the,x,y,z}$ respectively. The ambient magnetic field is $|\tilde{B}_0| = 1.5$. The shock has an averaged Alfvénic Mach number, $M_A = V_{shock}/V_A = 5.14$ where the upstream Alfvén velocity $\tilde{V}_A$ is equal to 0.075. The ratio β of upstream plasma thermal pressure to magnetic field pressure is taken as $\beta_i = 0.101$ for protons and $\beta_e = 0.16$ for electrons. For these initial conditions, all other upstream plasma parameters are detailed in Table 1 for both electrons and protons.

[10] Second, we follow the full motion of test-particle ions interacting with the electromagnetic fields of a shock profile issued from the above PIC simulation at a fixed time. A total of 51200 ions are used in each test particles simulation. In order to avoid any possible impact of the numerical noise (source of artificial particles diffusion before the particles interact with the shock front), all shock profiles issued from 2-D PIC simulations have been partially filtered in the upstream region (ahead of the upstream edge of the foot). In order to analyze the impact of a varying initial kinetic energy, the distribution of the test ions velocities is initially described as a shell function, and ions only differ by their phase angles (θ and ϕ) on the shell. As illustrated in Figure 1a, the gyrophase angle ϕ is defined as the angle between the + x direction (along the shock front normal) and the perpendicular ion velocity component $V_{i\perp}$ (defined with respect to the ambient magnetic field B_0), while the pitch angle θ is the angle between the ion velocity vector V_i and B_0. Test particles are produced by using acceptance-rejection method [*Knuth*, 1981] and are uniformly distributed on the shell. All particles have the same initial kinetic energy defined by the shell radius as shown in Figure 1b. Shell distributions of ions are released with different shell radii varying from

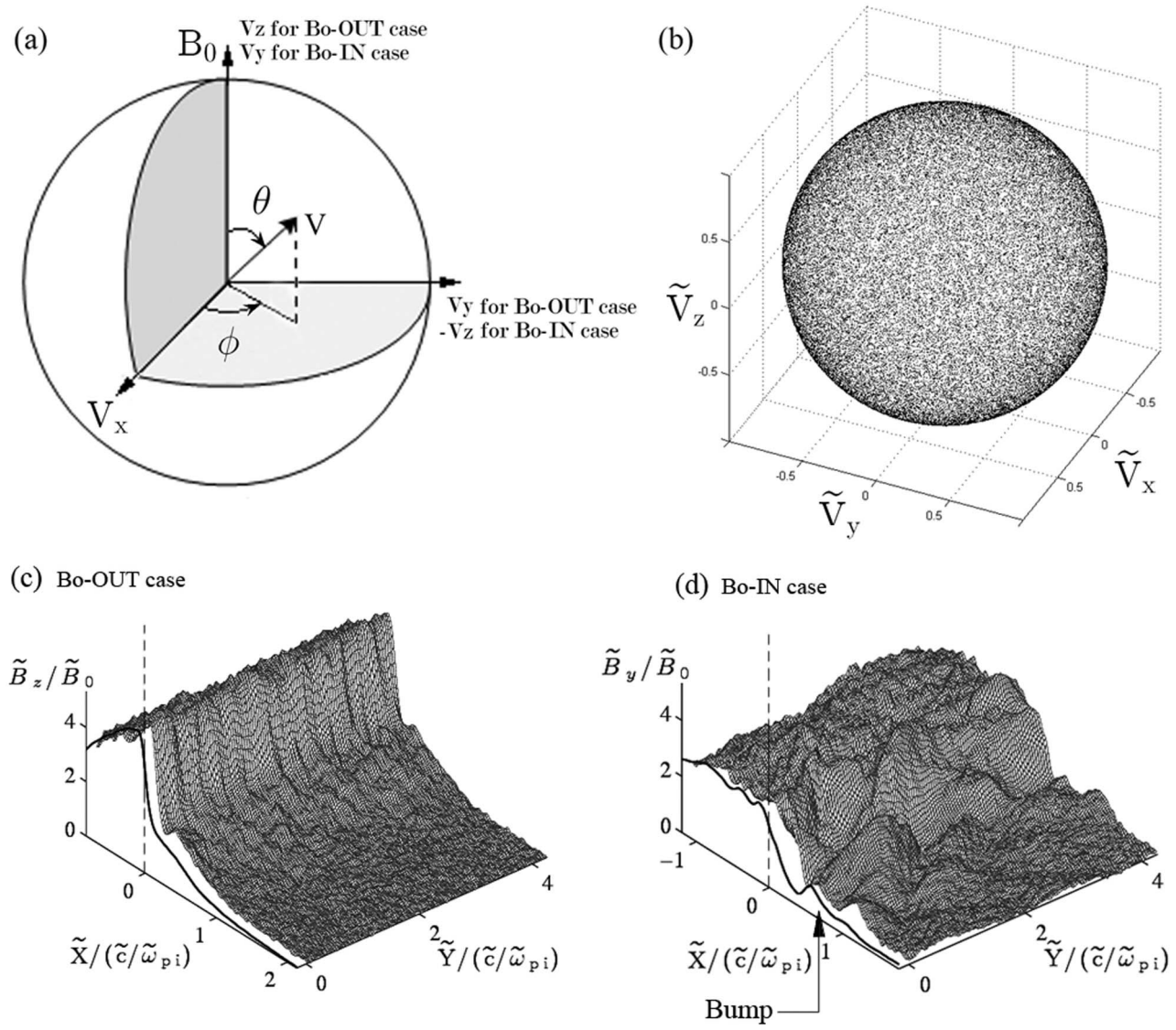

Figure 1. (a) Sketch of the injection angles of incident ions defined in the test particle calculations, (b) the test particles produced by acceptance-rejection method are uniformly distributed in the velocity shell, and (c) three-dimensional view of the main magnetic field component $\tilde{B}_z$ in unit of the upstream ambient magnetic field $\tilde{B}_0$ (B_0-OUT case) and (d) of $\tilde{B}_y$ also in unit of $\tilde{B}_0$ (B_0-IN case) issued from 2-D PIC simulations at the same time $\tilde{t} = 0.7\tilde{\tau}_{ci}$. The y-averaged shock profile (thick curve) is also shown for reference. Test particles simulations are made in the upstream rest frame. For clarity, the location of the ramp (where the electric field $\tilde{E}_x$ is maximum) has been chosen as the reference origin for plotting x-profiles of fields in Figures 1c and 1d (and in all other figures).

$\tilde{V}_{shell} = \tilde{V}_{thi}$ to $10\tilde{V}_{thi}$, where $\tilde{V}_{thi}$ is the proton thermal velocity used in our PIC simulation. Herein, we will consider protons (H^+) only. Test particles are initially distributed from a location $5\tilde{c}/\tilde{\omega}_{pi}$ away from the ramp to far upstream, and simulations are performed in the upstream rest frame. Since periodic conditions have been used along y-axis in original 2-D PIC simulations ($\tilde{L}_y = 256$), one can easily extend the shock profiles domain in the test particles simulations by duplicating all fields along y-axis in order to analyze in details carefully the full motion of DT, SDA and SSA ions along the shock front, which could be larger than $\tilde{L}_y = 256$.

3. Simulation Results

[11] This section is separated into two parts. In the first part, we analyze the dynamics of ions interacting with typical y-averaged shock profiles issued both from B_0-OUT and B_0-IN cases. Herein, the propagating shock is injected with an instantaneous velocity equaling that measured in the PIC

simulation; let us remind that the instantaneous Mach number may differ from its time-averaged value $M_A = 5.14$. For B_0-OUT case, the self-reformation is fully recovered associated with the absence of any whistler wave emission, and the shock front ripples have a small spatial scale along the shock front (Figure 1c) as in previous papers [*Lembège and Savoini*, 1992; *Lembège et al.*, 2009]. In contrast, for B_0-IN case, emission of whistler waves is evidenced associated with the absence of self-reformation as in previous papers [*Hellinger et al.*, 2007; *Lembège et al.*, 2009] and the shock front ripples have scales much larger than for the B_0-OUT case (Figure 1d). In the second part, we follow a similar procedure for non-averaged shock profiles issued from both B_0-OUT and B_0-IN cases. In each part, the analysis is based on a comparison between B_0-OUT and B_0-IN cases where shock front rippling is respectively excluded and included, i.e., with y-averaged (i.e., front rippling excluded) and non-averaged (i.e., front rippling included) shock profiles in order to answer the questions addressed in this paper and mentioned in section 1.

3.1. Dynamics of Ions Interacting With Y-Averaged Shock Profiles in "Bo-OUT" and "Bo-IN" Configurations

[12] Figure 1c shows the magnetic field strength $\tilde{B}_z(x,y)$ (in unit of $\tilde{B}_0$) at time $\tilde{t} = 0.7\tilde{\tau}_{ci}$ of the 2-D PIC simulation (where $\tilde{\tau}_{ci} = 2\pi/\tilde{\Omega}_{ci}$ is the upstream ion cyclotron period). The shock front rippling has a small spatial scale ($\sim 0.35\tilde{c}/\tilde{\omega}_{pi}$) along the y direction; B_0 is along z direction in the current case. The black solid curve indicates the corresponding y-averaged shock profile of $\tilde{B}_z$. In this y-averaged profile, the shock front clearly exhibits a foot, a ramp and an overshoot, which are typical characteristics of supercritical perpendicular shocks. The vertical dashed line indicates the ramp location (where the $\tilde{E}_x$ field has the largest amplitude); its instantaneous propagating velocity along x direction is $\tilde{V}_{shock} = 4.31\tilde{V}_A$ ($\sim 26.9\tilde{V}_{thi}$). Its shock front width (including foot and ramp) is about $1.9\tilde{c}/\tilde{\omega}_{pi}$, and is measured from the upstream edge of the foot to the peak of the magnetic overshoot; the upstream edge of the foot is defined as the location where the magnetic field has increased by 6.67% over its upstream value [*Burgess et al.*, 1989; *Yang et al.*, 2011a, 2011b]. The amplitude of the upstream magnetic field turbulence is below the value $(1 + 6.67\%) \times \tilde{B}_0$ in our simulations. At this chosen time of the PIC simulation, the ramp width is very narrow (about 2.4 $\tilde{c}/\tilde{\omega}_{pe}$), and is measured from the upstream edge of the ramp to the overshoot. Such a very narrow ramp is expected to be in favor of SSA mechanism [*Zank et al.*, 1996; *Lever et al.*, 2001]. Correspondingly, the magnetic field strength $\tilde{B}_y(x, y)$ (in unit of $\tilde{B}_0$) is shown for the B_0-IN configuration in Figure 1d at the same time as Figure 1c. The shock front rippling has a larger spatial scale ($\sim 1.42\tilde{c}/\tilde{\omega}_{pi}$) along the y direction; B_0 is along the y direction in the current case. The black solid curve indicates the corresponding y-averaged shock profile of $\tilde{B}_y$. The vertical dashed line indicates the ramp location (where the $\tilde{E}_x$ field has the largest amplitude). Instantaneous shock velocity along x direction is $\tilde{V}_{shock} = 4.17\tilde{V}_A$ ($\sim 26\tilde{V}_{thi}$). Since the shock velocity is slightly different in both $\tilde{B}_0$ configurations, for a better comfort the ramp location will be used as a reference origin as illustrated in Figures 1c and 1d and in all plots versus x throughout the paper.

[13] Incident ions interacting with the shock front can be separated into five groups by using a separation method developed in previous work [*Lever et al.*, 2001; *Yang et al.*, 2009a]. More specifically, we first separate the upstream ions into two groups: the reflected (R) ions and the directly transmitted (DT) ions, and we analyze their dynamics separately. The reflected ions are identified as follows: after being reflected (1) their velocity component $\tilde{V}_{ix}$ is larger than the shock front velocity $\tilde{V}_{shock}$ (along the x axis), and (2) they are located upstream the ramp ($\tilde{X}_i > \tilde{X}_{ramp}$). Second, the R ions can be divided into two subpopulations by using a simple criteria [*Lever et al.*, 2001]: the SDA ions are identified as being primarily reflected by the Lorenz force, i.e., in the shock front these verify $\tilde{E}_x < \left(\tilde{V}_{iy}\tilde{B}_z - \tilde{V}_{iz}\tilde{B}_y\right)/\tilde{c}$. SDA ions do return upstream once before passing through the shock front. The SSA ions are identified as being primarily reflected by the electrostatic force, i.e., in the shock front these verify $\tilde{E}_x \geq \left(\tilde{V}_{iy}\tilde{B}_z - \tilde{V}_{iz}\tilde{B}_y\right)/\tilde{c}$. Finally, we tag each SSA particle during its flight through the simulation box, keeping the time history of its trajectory and recording the number of reflections. The SSA ions reflected once and more than once are respectively named "SSA-O" and "SSA-M", where "O" and "M" holds respectively for "once" and "multiple". Simultaneously, we also classify the SDA ions into two types: "SDA-C" and "SDA-NC", where "C" an "NC" hold respectively for "crossing" and "not crossing". The return of "SDA-C" ions transits across the shock front, i.e., their turning point is behind the overshoot. In contrast, the "SDA-NC" ions do not pass through the overshoot during the reflection, i.e., their turning point is before the overshoot. It is important to precise that, when applying the criteria mentioned above (in particular the criterium $\tilde{X}_i > \tilde{X}_{ramp}$), the turning point of SDA and SSA ions can take place anywhere within the front without any a priori idea as illustrated in Figure 2. Even an ion which has its turning point behind the ramp (as the yellow curve) but succeeds to be ahead of the ramp after turning toward upstream and to reach the vertical dashed area will be selected as reflected ion.

[14] Figures 3a and 3b show the ion phase space $\tilde{V}_{ix}$ versus $\tilde{X}$ with three different initial shell radii $\tilde{V}_{shell} = 1$, 5 and $10\tilde{V}_{thi}$ from top to bottom in each column, for the B_0-OUT and B_0-IN configurations, respectively. The essential differences between the y-averaged shock profiles of both cases are the following: (1) the gradient of the shock front (in particular at the ramp) is much weaker (lower fields amplitude at the shock front, and thicker front width) in B_0-IN case than in B_0-OUT case (Figures 1c and 1d); (2) the fields within the foot vary monotonously versus x in B_0-OUT case, in contrast with those of B_0-IN case where a "bump" is clearly evidenced upstream of the ramp (as indicated by the arrow in Figure 1d). The amplitude of this bump is not negligible and will have a noticeable impact according to the initial energy and injection features of some ions interacting with it.

[15] Spatial coordinates are in unit of upstream ion inertial length $\tilde{c}/\tilde{\omega}_{pi}$. The five groups of ions are identified and are color-coded as follows: (1) reflected SDA-C ions (cyan

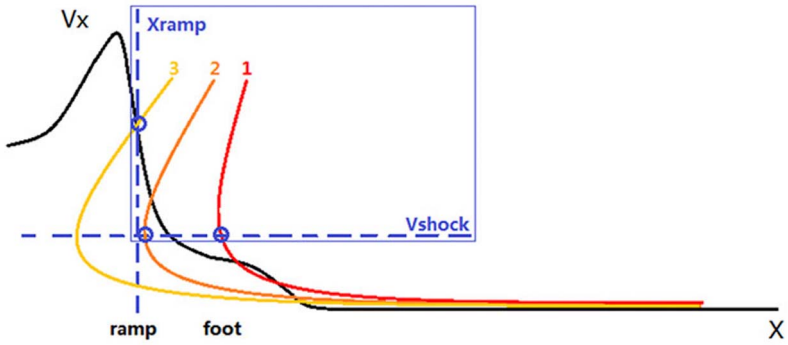

Figure 2. Sketch of typical reflected ion trajectories. The red, orange and yellow curves illustrate respectively trajectories of an SSA/SDA ion reflected within the foot, at the ramp and of an SDA ion reflected after the overshoot (herein so-called SDA-C ion); the blue circles indicate the location where the incident ion is defined as reflected, and is classified into SSA and SDA groups by using the criteria described in the text.

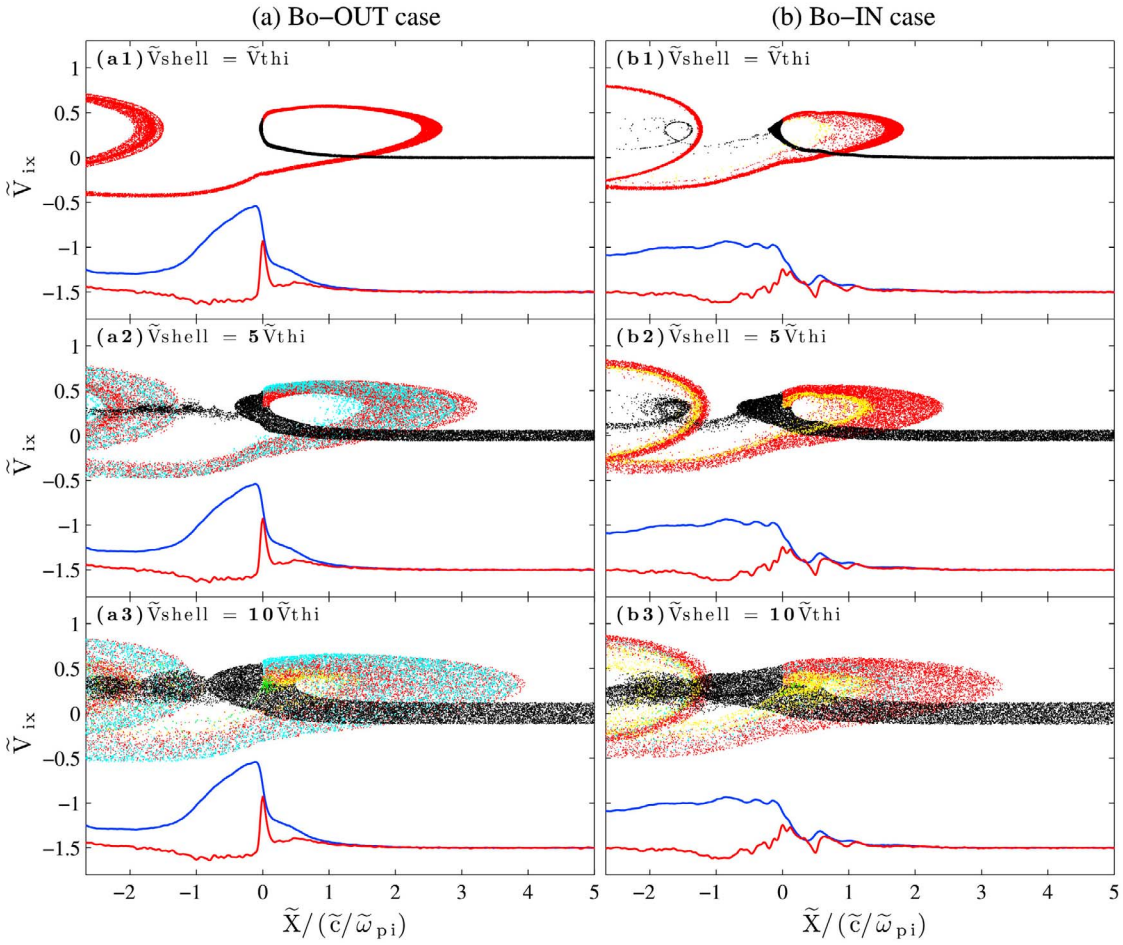

Figure 3. Ion phase space ($\tilde{V}_{ix} - \tilde{X}$) issued from 2-D test particles simulations for three different initial shell velocities $\tilde{V}_{shell} = 1$, 5 and $10\tilde{V}_{thi}$ for the y-averaged shock profiles in (a) B_0-OUT and (b) B_0-IN configurations. Spatial coordinates are normalized versus the upstream ion inertial length $(\tilde{c}/\tilde{\omega}_{pi})$. Colors are as follows: incoming and DT ions (black), SDA-C ions (cyan), SDA-NC ions (red), SSA-O ions (yellow) and SSA-M ions (green). For reference, the y-averaged fields of the shock profile $\tilde{B}_z$ (blue curve) and $\tilde{E}_x$ (red curve) are also shown for reference; the ramp location is chosen as the origin $\tilde{x} = 0$ of the plot.

dots), (2) reflected SDA-NC ions (red dots), (3) reflected SSA-O ions (yellow dots), (4) reflected SSA-M ions (green dots), and (5) DT ions together with incoming ions (black dots). Corresponding profile of the y-averaged magnetic field $\tilde{B}_z$ (blue curve) and electric field $\tilde{E}_x$ (red curve) are also shown for reference in Figure 3. Main results are as follows:

[16] 1. For small shell cases (Figure 3a1), DT and SSA-O ions are absent for B_0-OUT configuration (i.e., all ions are reflected). In contrast, for B_0-IN configuration, DT and SSA-O ions emerge. The increase of DT ions percentage is easily explained by the fact that the shock front amplitude (overshoot) is much lower in Figure 3b than in Figure 3a; as a consequence, the reflection is less efficient and the extension of the reflected ions into the upstream region is more restricted (Figure 3b).

[17] 2. For middle $\tilde{V}_{shell}$ cases, SDA-C ions become noticeable and DT ions emerge for B_0-OUT configuration (Figure 3a2), while the relative percentage of SSA-O and DT ions drastically increases for B_0-IN configuration (Figure 3b2).

[18] 3. For large $\tilde{V}_{shell}$ cases, whatever is the shock profile, more SSA ions are evidenced. In addition, the upstream spatial range where reflected ions extend (both for SDA and SSA ions when these are evidenced) is larger as the $\tilde{V}_{shell}$ value increases. However, for B_0-IN configuration, the number of SDA-C ions increases (this feature will be analyzed later on). More generally, when crossing the shock front, DT ions go downstream without any reflection, and get some bulk velocity only. In contrast, reflected ions are accelerated when interacting with the shock front and become the most energetic. Larger $\tilde{V}_{shell}$ value is in favor of producing more reflected (SSA and SDA-C) ions since these succeed to pass more easily through the shock front after interacting with it (acceleration).

[19] 4. SDA-NC ions are always evidenced whatever are the $\tilde{V}_{shell}$ value and the shock profile. The ion diffusion increases with large $\tilde{V}_{shell}$ (Figures 3a3 and 3b3) so that the coherent ion motion is destroyed and the vortex of reflected ions disappears.

[20] In order to identify more clearly the dynamics of the different ion populations and their differences between the B_0-OUT and B_0-IN configurations, time trajectories ($\tilde{Y}$-$\tilde{X}$ shown in shock rest frame) of four types of reflected ions suffering different energization mechanisms (SSA-O, SSA-M, SDA-C, and SDA-NC) are plotted in y-averaged cases. Let us consider the B_0-OUT configuration first (Figures 4a1–4a4). Black circle and crossing on the trajectory indicate respectively the beginning and the end of the trajectory. These particles do have the same initial kinetic energy since these are selected from the same shell distribution ($\tilde{V}_{shell} = 10\tilde{V}_{thi}$); these only differ from each other by the phase angles on the shell. Vertical dashed lines indicate the locations of the overshoot "O", the ramp "R" and the upstream edge of the foot "F" respectively. Isocontours of the magnetic field $\tilde{B}_z$ (in gray) are superimposed on the $\tilde{Y}$-$\tilde{X}$ plots as reference. Corresponding kinetic energy $\tilde{E}_k$ versus $\tilde{X}$ (calculated in simulation frame) is shown in Figures 4a5–4a8; kinetic energy $\tilde{E}_k$ is normalized to the initial injection kinetic energy defined by $\tilde{E}_{inj} = \tilde{m}_i\left(M_A\tilde{V}_A\right)^2/2$ (the instantaneous Mach number value $M_A = 4.31$ is used here). Y-averaged profiles of the magnetic field $\tilde{B}_z$ (grey thick curve) and electric field $\tilde{E}_x$ (grey thin curve) are also shown for reference.

[21] Figure 4a1 shows the trajectory of a typical SSA-O ion which is reflected mainly due to the electric field. One surprising result is that the particle only suffers one bounce within the foot instead of the ramp during its acceleration process. As a consequence, the energy gain is maximum within the foot ($\Delta\tilde{E}_k > 2\tilde{E}_{inj}$) and not at the ramp (Figure 4a5) and is relatively large (even if lower) as compared to the energy gain observed for SSA-M ion (Figure 4a6). One bounce of SSA-O ion reveals to be quite efficient, a fact which has not been analyzed in previous theoretical works to the knowledge of the authors. One proposed reason of the bouncing of SSA-O ion within the foot is the fact the local electric field amplitude (in the foot) has a finite value which is a certain percentage of the same field at the ramp. Then, the selection criterion for SSA ions can apply locally and one bounce is initiated. This result differs from previous models of SSA process where the electric field is often represented by one strong peaked gradient at the ramp for simplifying [*Zank et al.*, 1996; *Lee et al.*, 1996; *Shapiro and Üçer*, 2003]. Figure 4a2 shows the trajectory of a SSA-M ion which suffers multireflection by the local longitudinal electric field mainly within the ramp. In contrast with SSA-O process, the behavior of SSA-M particle is very close to that expected in previous theoretical model of shock surfing acceleration [*Lee et al.*, 1996; *Zank et al.*, 1996; *Shapiro and Üçer*, 2003]. These multireflected ions have already been found at a reforming shock in 1-D simulation [*Yang et al.*, 2011b] and are presently retrieved at 2-D shock profiles. As expected and in contrast with the SSA-O case, the energy gain of the SSA-M particle is the strongest at the ramp; this energy gain increases with the number of reflection at the ramp and is larger than that observed for SSA-O ion ($\Delta\tilde{E}_k = 2.8\tilde{E}_{inj}$ in Figure 4a6). Figure 4a3 shows a standard SDA-C ion which describes a large gyromotion during its reflection. Herein, its turning point is behind the ramp (and even behind the overshoot). One main feature is that its energy gain is very large at its turning point in the downstream region and reaches its maximum value ($\Delta\tilde{E}_k = 3.8\tilde{E}_{inj}$ in Figure 4a7) as the particle reaches its maximum excursion far in the foot region at location "F" (i.e., before coming back definitively to the shock front). Figure 4a4 shows the SDA-NC ion which describes a gyromotion during its acceleration. Herein, the turning point is within the foot i.e., before reaching the ramp. Its corresponding energy gain is maximum again at location "F" at the foot but is lower than that observed for SDA-C. This means that the energy gain observed in the downstream region for the SDA-C ion (immediately after crossing the ramp) plays an important role and largely contributes to the final energy gain. Indeed and in contrast with SDA-C ion, the SDA-NC does not suffer any acceleration when crossing the ramp or the overshoot region for the first time. A striking point is that SDA process is dominant in the sense that the resulting energy gain is the largest among the different cases concerned herein.

[22] The four different classes of ions are also identified for B_0-IN configuration as illustrated in Figure 4b, and within each ion class, features similar to those identified for B_0-OUT persist. The instantaneous Mach number value

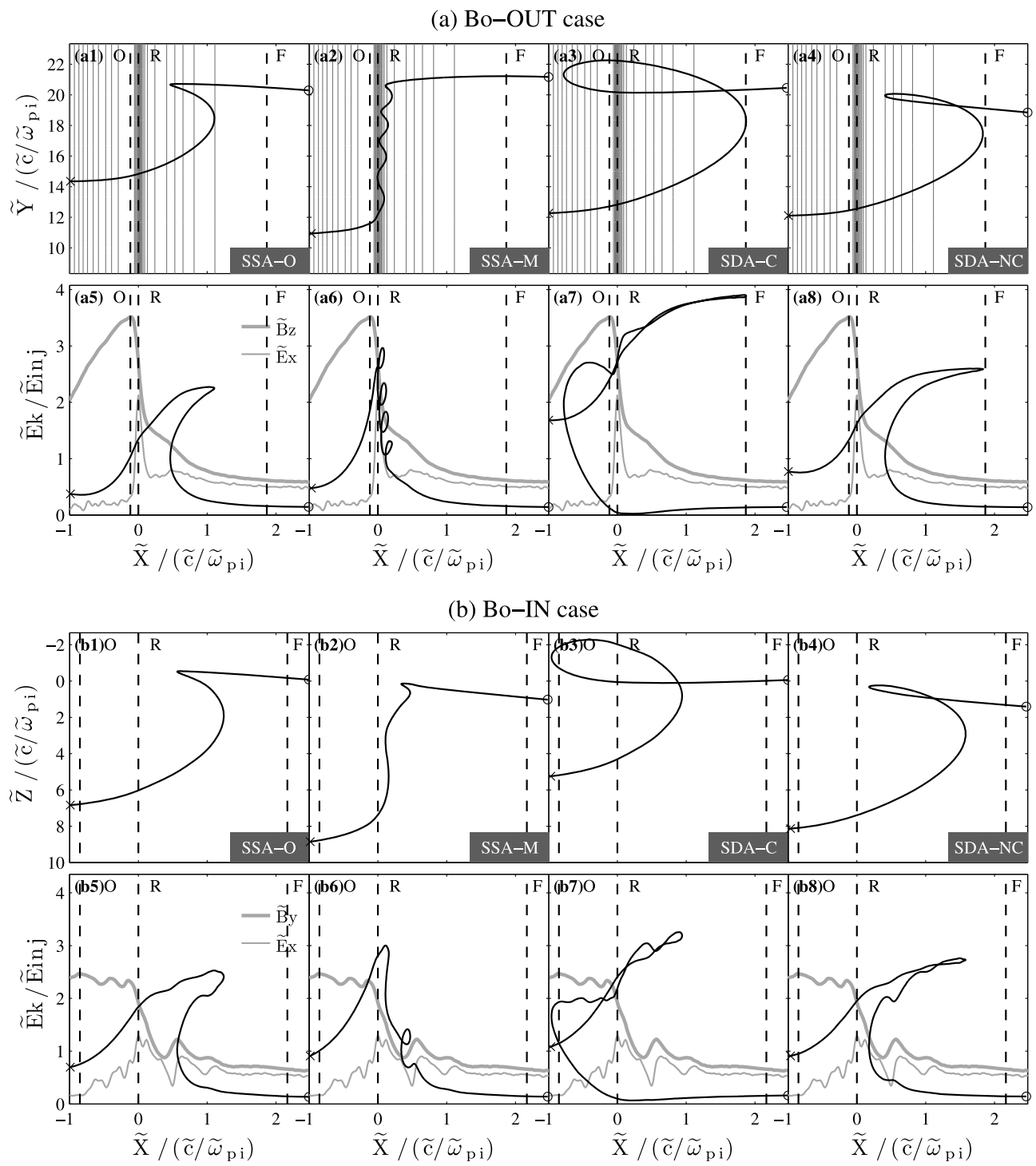

Figure 4. (a) Time trajectories ($\tilde{Y} - \tilde{X}$) of four typical reflected ions issued from test particles simulations performed for the y-averaged case defined for the "B_0-OUT" configuration: SSA-O, SSA-M, SDA-C and SDA-NC ions are shown in Figures 4a1–4a4, respectively. Small black circle and crosses on each trajectory indicate the beginning and the end of the ion trajectory. The ramp location is chosen as the origin $\tilde{x} = 0$ of the plot. Curves are defined for the same initial shell velocity $\tilde{V}_{shell} = 10/\tilde{V}_{thi}$. Isocontours curves of $\tilde{B}_z$ are superimposed in Figures 4a1–4a4 for reference. The shock profile is defined at time $\tilde{t} = 0.7\tilde{\tau}_{ci}$ of the 2-D PIC simulation. Corresponding normalized kinetic energy $\tilde{E}_k/\tilde{E}_{inj}$ versus $\tilde{X}/(\tilde{c}/\tilde{\omega}_{pi})$ is shown in Figures 4a5–4a8, where the injection kinetic energy $\tilde{E}_{inj} = \tilde{m}_i(M_A\tilde{V}_A)^2/2$; the y-averaged profiles of $\tilde{B}_z$ and $\tilde{E}_x$ are also shown for reference. Vertical thick dashed lines from left to right indicate the locations of the overshoot "O", the ramp "R" and upstream edge of the foot "F" respectively. (b) Similar plots for "B_0-IN" configuration.

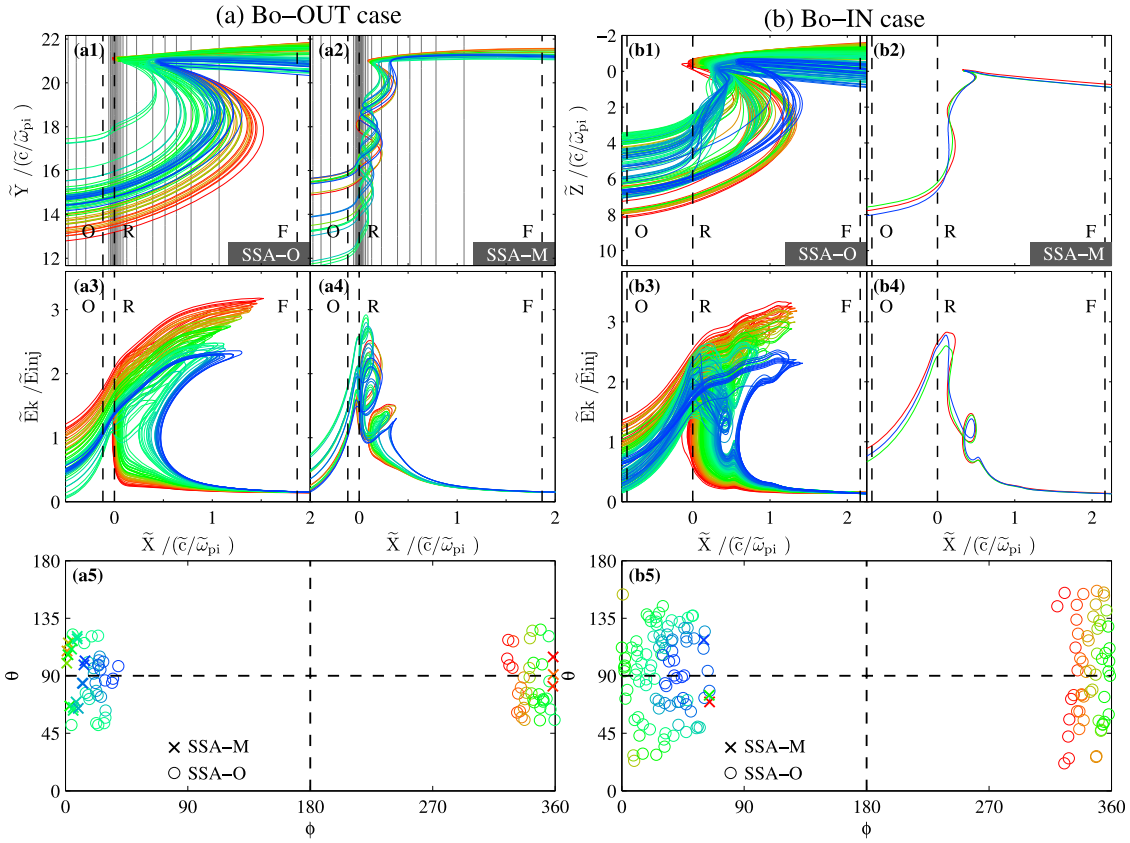

Figure 5. (a) Plots similar to those of Figure 4 but focused on different reflected ions (different colors) suffering SSA-O (Figure 5a1) and SSA-M (Figure 5a2) processes (for the y-averaged B_0-OUT configuration and for $\tilde{V}_{shell} = 10\tilde{V}_{thi}$). Vertical dashed lines from left to right indicate the locations of the overshoot "O", the ramp "R" and the upstream edge of the foot "F" respectively. Corresponding normalized kinetic energy $\tilde{E}_k/\tilde{E}_{inj}$ versus $\tilde{X}/(\tilde{c}/\tilde{\omega}_{pi})$ is shown in Figures 5a3 and 5a4, where the injection kinetic energy is $\tilde{E}_{inj} = \tilde{m}_i(M_A\tilde{V}_A)^2/2$. The ramp location is chosen as the origin $\tilde{x}$ = 0 of the plot. Figure 5a5 shows the domains of velocity injection angles ($\theta - \phi$) of SSA-O (circle) and SSA-M (cross) ions. (b) Similar plots for the y-averaged B_0-IN case.

M_A = 4.17 is used herein. However, a few differences can be stressed between both B_0 configurations: the number of bounces of the SSA-M ion can be larger in Figure 4a2 than in Figure 4b2, then one could expect the kinetic energy gain be higher too. In fact, this expectation is in disagreement with present result as seen by comparing Figures 4b6 and 4a6 which show comparable energy gain. This can be explained by the fact that the SSA-M ion in Figure 4b2 does not stay within the ramp which is believed to be a necessary condition to suffer multiple bounces allowing to get a large energy gain [*Shapiro and Üçer*, 2003] as evidenced in Figure 4a6. Instead, the SSA-M ion of Figure 4b6 first interacts with the upstream bump (located in the foot region and indicated by the arrow in Figure 1d), suffers one bounce and then interacts with the ramp that it succeeds to cross.

[23] Figure 5 shows the trajectories of SSA-O and SSA-M ions coming from the same shell velocity distribution with shell radius $\tilde{V}_{shell} = 10\tilde{V}_{thi}$; all ions have the same initial energy. Ions have been selected randomly (from their shell distribution shown in Figure 1b) among the 51200 ions used in each simulation. This allows us to investigate the behavior of the SSA ions within the shock front in more detail. Figures 5a and 5b indicate the results obtained in B_0-OUT and B_0-IN configurations respectively. For each case, results for SSA-O and SSA-M ions are respectively plotted in Figures 5a1, 5b1 and Figures 5a2, 5b2; corresponding kinetic energy are plotted in Figures 5a3, 5b3, 5a4, and 5b4. More precisely, the trajectories of particles are color-coded according their turning point as the reflection of the particle takes place more deeply within the shock front as illustrated in Figures 5a1 and 5a2 (the choice of colors extends from blue to red, and gradually varies through the colors cyan, green, yellow, and orange). Let us remind that ions are distributed on the same shell and differ one from each other only by their respective phase angles. In present simulation, injection angles (gyrophase ϕ and pitch angle θ) of each selected particle have been recorded. Both angles start to be recorded as each ion first reaches the upstream edge of the foot.

[24] First, let us consider the B_0-OUT configuration. Figure 5a5 shows the domain in injection angles (θ-ϕ) of the velocity space for the incident ions undergoing the SSA-O (marked by circles) and SSA-M (marked by crosses) processes. The original distribution of these surfing ions is centered around the direction $\theta = 90°$ ($45° < \theta < 135°$) and

around the $\tilde{V}_{ix}$ axis ($320° < \phi < 360°$ and $0° < \phi < 40°$). Present results show that small change in angles lead to quite different SSA-O and SSA-M particles trajectories. For SSA-O ions, three groups of ions are considered and identified by blue ($0° < \phi < 40°$), red ($320° < \phi < 360°$) and green colors; "green" ions are distributed within the two other groups in terms of kinetic energy (Figure 5a3). When considering successively "blue", "green" and "red" ions, the reflection point of the SSA ions initially in the foot (blue ions), approaches (green ions) and reach (red ions) the ramp (Figure 5a1). Then, SSA-O ions are reflected within a relatively large x-domain either within the foot or at the ramp depending on their initial injection angle. The SSA-O ions reflected at the ramp always gain more energy than the SSA-O ions reflected within the foot (Figures 5a1 and 5a3); this is due to the fact that SSA-O ions see higher local electric field amplitude when approaching progressively the ramp. Second, let us consider the B_0-IN configuration. The trajectories are more complex since some ions interact with both the ramp and the "bump" located upstream of the ramp. For SSA-O ions (Figures 5b1 and 5b3), this is clearly apparent with "blue" and some "green" ions which describe a more intricate trajectory near the bump location. In contrast, the "red" ions which directly interact with the ramp do have trajectories and energy gain evolution more similar to those of "red" SSA-O ions for B_0-OUT configuration.

[25] For B_0-OUT configuration, the SSA-M ions interact within a more restricted x-domain near the ramp (Figure 5a2) in contrast with SSA-O ions. The first turning point of SSA-M ions is initially within the foot edge located near the ramp ("blue" ions), and approaches progressively the ramp ("green" and "red" ions) but do not reach it. These reach the ramp after several reflections only. The SSA-M ions which spend more time in the ramp (either by more reflections or by combining less reflections and by increasing their y-excursion path along the shock front during each reflection) do have the largest energy gain, as the "green" ions do in Figures 5a2 and 5a4. The SSA-M ions which are reflected early (i.e., with turning point in the foot far from the ramp as some "blue" ions) do not have maximum energy gain. Then, an early reflection is not in favor of getting a better energy gain; instead, the relative proximity to the ramp is rather in favor. One striking feature is that some SSA-O ions can reach a final maximum energy gain comparable to (and even slightly larger than) that of the SSA-M ions. This maximum energy gain takes place far from the ramp (near the foot edge "F") for SSA-O ions and within the ramp for SSA-M ions respectively ($\Delta\tilde{E}_k = 3$ and $2.8\tilde{E}_{inj}$ respectively in Figures 5a3 and 5a4. Moreover, Figure 5a5 shows that SSA-M ions (marked by crosses) are "surrounded" by SSA-O ions (marked by circles), and are more centered around the direction $\theta = 90°$. SSA-O ions come from the domain between SDA domain (it will be analyzed in detail in Figure 8) and SSA-M domain (i.e., $\theta \sim 90°$ and $\phi \sim 360°$ or $0°$ and are in a good agreement with theoretical results of *Shapiro and Üçer* [2003]) due to the continuously changing of injection angles of the incident ions from a same shell. In order to compare with theoretical results of *Shapiro and Üçer* [2003], we have plotted in Figure 6 the number of bounces versus the $\tilde{V}_{ix,hit}$ velocity component (all velocity components have been transformed from the upstream frame to the shock rest frame for comparison) of SSA-M ions at the time these hit the upstream edge of the shock front (subscript "hit", in Figure 6a5). A good agreement is found between theoretical and simulation results which confirms that low $\tilde{V}_{ix,hit}$ velocity component is in favor of large number of bounces. Let us precise that particles with velocity approaching the maximum $\tilde{V}_{ix}$ in the upstream rest frame correspond to those with low initial velocity in the shock rest frame. This is illustrated in Figure 7 where an ion shell is represented in both shock rest frame (black coordinate system as mentioned by *Shapiro and Üçer* [2003]), and upstream frame (red coordinate system used in present simulations). In addition, Figure 6 provides several other information: (1) the number of bounces in present simulation is limited (maximum of about 4 bounces) with respect to theoretical expectations; (2) SSA-O ions which bounce respectively at the ramp (red circles) and far within the foot (blue circles) do have a larger and smaller $\tilde{V}_{ix,hit}$ respectively. This last result suggests that another parameter (in addition to $\tilde{V}_{ix,hit}$) needs to be invoked in order to separate SSA-O (green and blue circles) and SSA-M (red crosses) which co-exist within the same $\tilde{V}_{ix,hit}$ range (0.197–0.216 in Figure 6a5). In order to clarify this point, time histories of ion components velocities $\tilde{V}_{ix}$ and $\tilde{V}_{iy}$ are plotted in Figures 6a1–6a4 with the same color code as used for each identified particle in other plots in Figure 5. The time at which each ion is bouncing (which is characterized by $\tilde{V}_{ix} = 0$) differs from the (previous) time at which the ion starts to interact with the shock front (as indicated by the circle on each ion trajectory in Figures 6a1–6a4. These plots clearly show that: (1) at the time these interact with the shock front, SSA-O ions spread over a certain finite range of $\tilde{V}_{ix}$ and $\tilde{V}_{iy}$ velocity components, while this range is almost zero for SSA-M (all circles almost superimpose one to each other). This feature explains the reason for which SSA-M ions look "surrounded" by SSA-O ions; (2) at their turning point, the $\tilde{V}_{iy}$ is small but finite for SSA-M ions but is almost zero for SSA-O ions. Then, a small finite or $\tilde{V}_{iy} = 0$ component will decide whether the SSA ion will be an SSA-O or SSA-M. This new result (impact of $\tilde{V}_{iy}$) was not expected from theoretical results of *Shapiro and Üçer* [2003]. This dependance versus $\tilde{V}_{iy}$ (i.e., ϕ angle) is due to the continuous gyration that all incident ions (and then of the whole shell distribution) around $\tilde{B}_0$ axis (z-axis) suffer when approaching the shock front.

[26] For B_0-IN configuration, several differences emerge with respect to the B_0-OUT configuration: (1) the number of bounces for SSA-M ions (Figure 5b2) is much more reduced as compared to Figure 5a2, which can be explained as follows: the gradient of the shock front at the ramp is much weaker (lower electric field $\tilde{E}_x$ and thicker front width) in B_0-IN case than in B_0-OUT case. Let us remind that the number of bounces increases in particular in the region where the ramp is very thin (a few electron inertia lengths) as in Figure 5a, which is in agreement with the model of *Shapiro and Üçer* [2003]. The maximum energy achieved by both classes of SSA ions (Figures 5b3 and 5b4) are almost comparable to that of Figures 5a3 and 5a4; (2) The presence of a "bump" along x-axis disturbs trajectories of ions which suffer some diffusion (as compared with the monotonic increase of the fields amplitude in B_0-OUT configuration). This diffusion is due to the fact that the particles

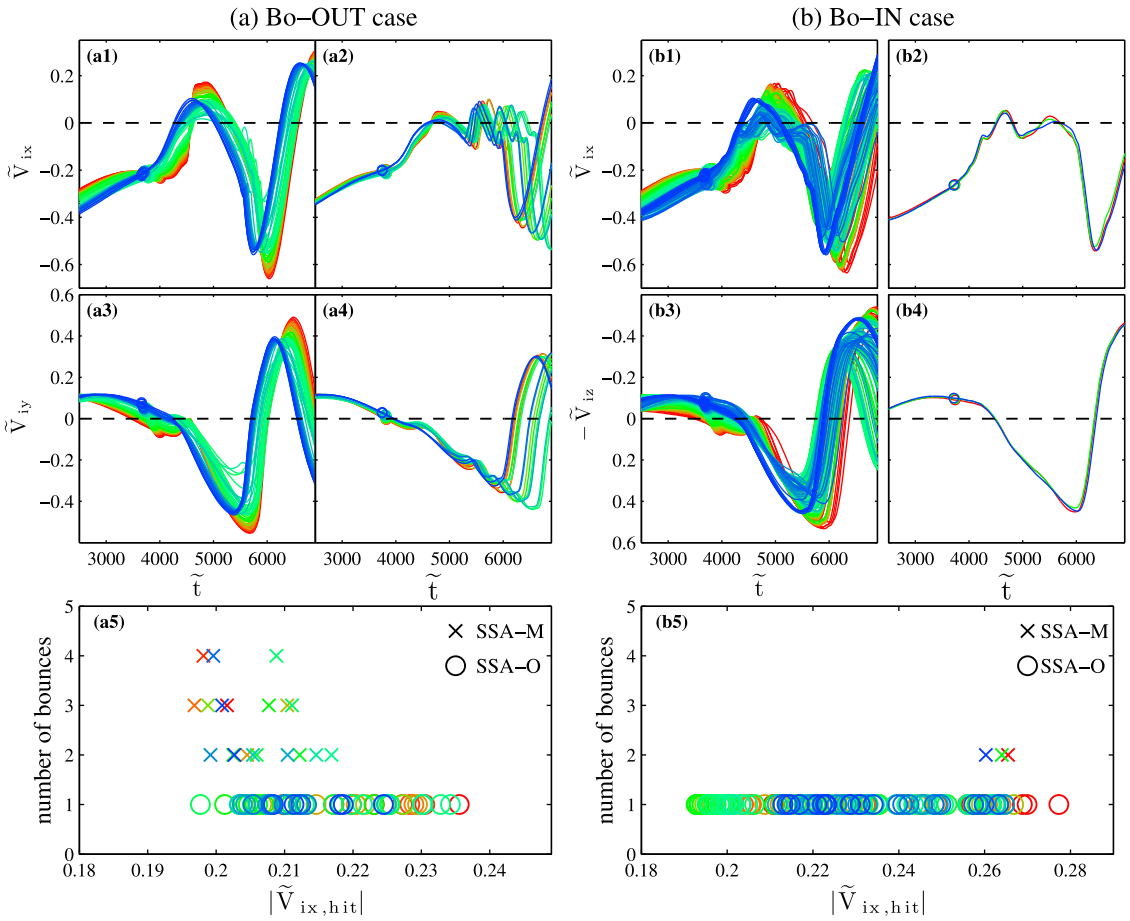

Figure 6. (a) Corresponding time history of $\tilde{V}_{ix}$ and $\tilde{V}_{iy}$ injection velocity components of ions selected in Figures 5a1–5a4 for the "B_0-OUT" case; same color code is used. Circles on each curve denote the "hitting time" (denoted by subscript "hit") at which the particle starts interacting with the upstream edge of the shock front; the number of bounces for each ion is reported in Figure 5a5 versus the $\tilde{V}_{ix,hit}$ velocity component measured at the hitting time (circles: SSA-O, crossings: SSA-M). (b) Similar results for the "B_0-IN" case. In order to compare with theoretical results of *Shapiro and Üçer* [2003], all velocity components of SSA ions presented here have been transformed from the simulation frame (i.e., upstream frame) to the shock rest frame.

interact at different locations upstream from and at the ramp, and see different local amplitudes of fields (including the upstream bump). This diffusion leads to an expansion of the angular domain in Figure 5b5 with respect to the domain of Figure 5a5; (3) considering the same sampling of ions selected in each configuration, the number of SSA-M ions (crosses) decreases strongly with respect to the B_0-OUT configuration and mainly SSA-O ions (circles) are identified in Figure 5b5. Then, weaker gradients of shock front profiles should be in favor of SSA-O ions. Moreover, Figure 6b confirms that small $\tilde{V}_{ix,hit}$ values reveal not to be the primary condition for producing SSA-M ions with many bounces, since SSA-O ions are rather evidenced; rather, a gradient of the electric field strong enough with a narrow ramp is the major condition (not satisfied in the B_0-IN configuration). Surprisingly, SSA-M ions with very limited number of bounces (only 2 in the present case) are observed for high $\tilde{V}_{ix,hit}$ values in Figure 6b5. At this stage, no further comparison can be performed with results of *Shapiro and Üçer* [2003] because of too much simplifying conditions used in the theoretical model while, in present test simulations, these ions are reflected within the foot region which was excluded in the previous model. A more realistic theoretical model will be necessary to analyze in further details the particular trajectories of SSA-M/SSA-O and SDA-C/SDA-NC ions interacting with the microstructures of the shock profile and different gradients of shock front. Such analysis will be presented in a further work.

[27] At this stage of the study, the analysis of individual trajectories is not enough and a full statistical analysis reveals to be necessary. Figure 8a shows the injection angles distribution for all SSA-O (yellow), SSA-M (green), SDA-C (cyan), SDA-NC (red), and DT (black) ions respectively for the three different radii of the initial shell distribution used in Figures 3a and 3b. For B_0-OUT configuration case, the main results are summarized as follows: (1) the frontiers of angular domains between the different ion classes are clearly identified; (2) for small shell cases ($\tilde{V}_{shell} = \tilde{V}_{thi}$), all ions are

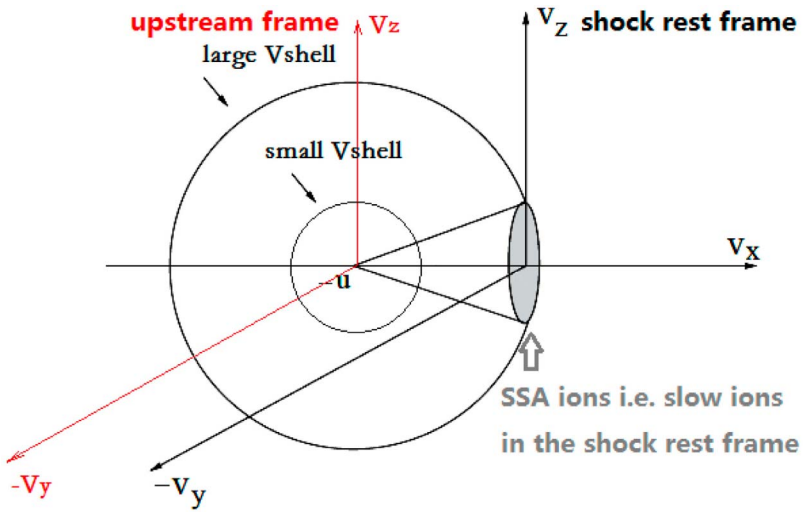

Figure 7. Sketch of low initial energy/weak ion velocity component V_x (in grey) in the shock rest frame (black coordinate system) mentioned by *Shapiro and Üçer* [2003]. These ions correspond to those with velocities approaching the maximum $\tilde{V}_{ix}$ in large $\tilde{V}_{shell}$ case in the upstream rest frame (red coordinate system) used in present simulations. Sketch inspired from *Shapiro and Üçer* [2003, Figure 4].

reflected; SDA-NC ions dominate everywhere and no SSA ions are identified (Figure 8a1); (3) for middle shell case ($\tilde{V}_{shell} = 5\tilde{V}_{thi}$), SDA-C and DT ions emerge and are mainly distributed in the right half of the plot ($160° < \phi < 300°$) in Figure 8a2; no SSA ions emerge yet; (4) for large shell cases ($\tilde{V}_{shell} = 10\tilde{V}_{thi}$), two new features appear: the domains of SDA-C and DT ions are expanding, and SSA ions emerge in such a way that SSA-M ions are located within a narrow angular range ($50° < \theta < 130°$ and $0° < \phi < 20°$) and are mainly "surrounded" by SSA-O ions (Figure 8a3) which confirms a feature mentioned in Figure 5a5. A more convincing illustration is shown in the 3-D plot of the angles distribution over the shell in Figure 9. As expected, these results are quite similar to those mentioned in previous 1-D simulations [*Lever et al.*, 2001; *Yang et al.*, 2009a] and theoretical model [*Shapiro and Üçer*, 2003]. Present results stress that most SSA ions come from the large shells and their injection velocities are nearly along the direction of the shock normal (along x-axis), in agreement with the results of *Shapiro and Üçer* [2003]. In addition, present results precise that large $\tilde{V}_{shell}$ are in favor for getting more SSA ions, and that the injection angular domain of SSA-O ions (yellow) represents a transition between SSA-M domain (green) to SDA domain (red) as clearly illustrated in Figure 9, a fact which will require a theoretical development in a further work. Some differences appear for the B_0-IN configuration (Figure 8b) and may be summarized correspondingly for a same given $\tilde{V}_{shell}/\tilde{V}_{thi}$ ratio as follows:

[28] 1. The domains of SDA-C ions (cyan) become more restricted in Figure 8b as compared to those of Figure 8a; this can be explained by the fact that SDA-C ions may have more difficulties to overcome the overshoot in order to describe their large gyromotion since some can interact first with the bump located upstream of the ramp and initiate a different reflection process. Let us remind that, among the different ion populations, the SDA-C ion corresponds to the reflected ion which performs a maximum penetration within the shock front to initiate a large gyration orbit.

[29] 2. In contrast, the domains of SSA-O (yellow) and DT (black) ions are larger and greatly expand. Indeed, as expected, a weaker fields gradient at the shock front (B_0-IN case) will help the formation of DT ions (because of the lower overshoot barrier), and will reduce the number of reflected ions. On the other hand, the increase of the SSA-O and SDA-NC angular domains is associated to ions interacting with the peaked bump upstream of the ramp. Indeed, Figure 5b3 shows that some ions suffer SSA-O process at the bump which plays the role of a small barrier (formation of ion vortex upstream of the ramp at the location of the bump); let us remind that the selection of the different types of SSA and SDA ions is performed within the front (section 3.1). In addition, Figure 8b evidence that the number of SSA-O ions interacting at different locations within the foot (peaked bump included) is quite high, which means that any non-monotonic variation of the shock profile from upstream to the overshoot may have a strong impact on the reflection process itself.

[30] 3. However, only a poor quantity of SSA-M can be identified for large $\tilde{V}_{shell}/\tilde{V}_{thi}$ ratio. Indeed, the presence of a thicker ramp (as in B_0-IN case) is not in favor of SSA-M process which requires a steeply narrow ramp in order to initiate efficient multibouncing.

[31] In summary, the reduction of reflected ions associated to B_0-IN case (and to the increase of DT ions) is mainly concerning SDA-C and SSA-M ions. The next step consists in determining more quantitatively the respective increase/decrease of ions density and energy loss/gain within the five ion classes identified in the downstream region at the end of the simulations. Then, a statistical study has been performed based on simulation runs carried out for 38 different shell radii $\tilde{V}_{shell}$ varying from 0.1 to $10\tilde{V}_{thi}$ in order to analyze more precisely the impact of initial conditions (variation of $\tilde{V}_{shell}$) for both B_0 configurations.

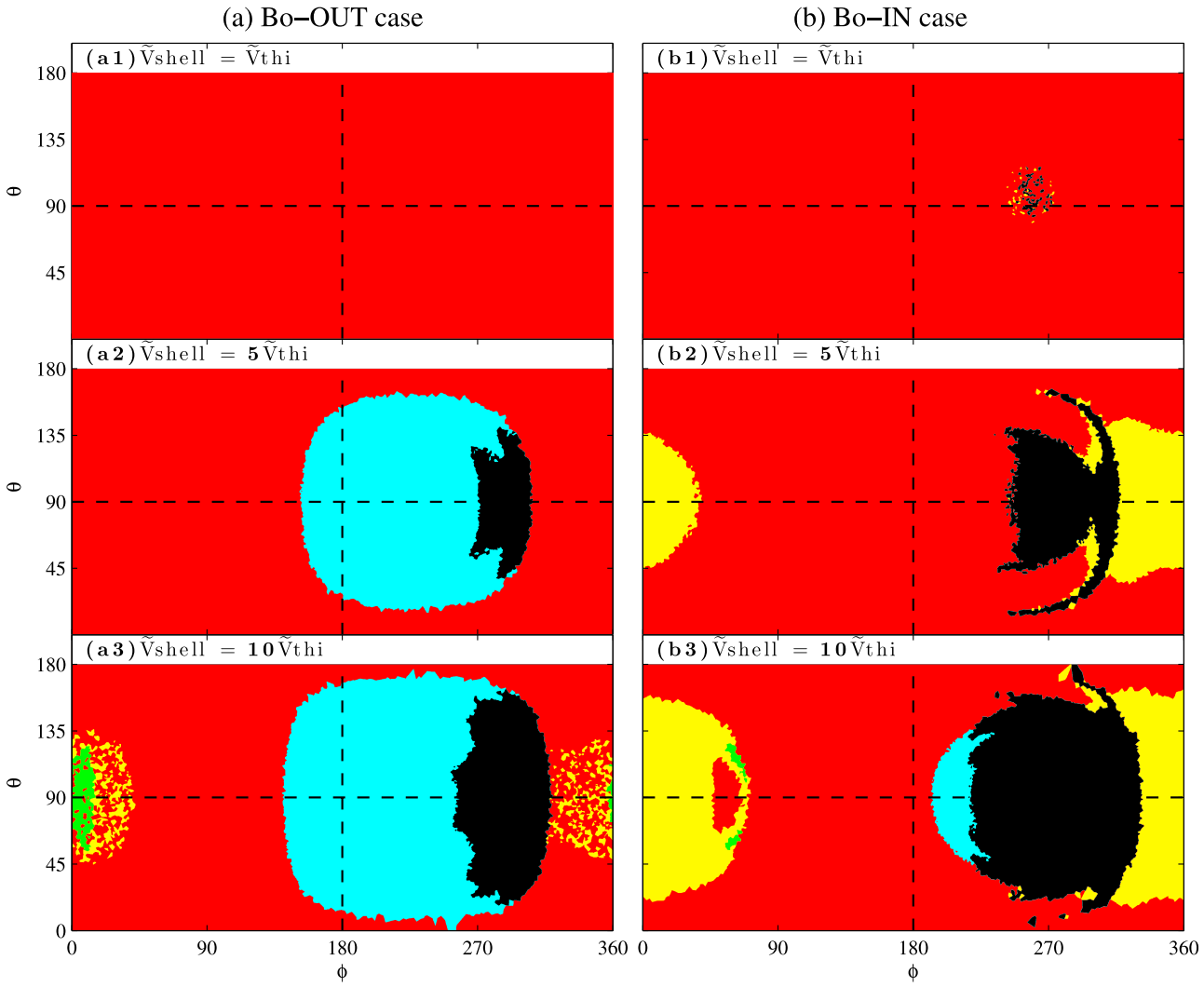

Figure 8. Domain of velocity injection angle ($\theta - \phi$) for DT (black), SDA-C (cyan) SDA-NC (red), SSA-O (yellow) and SSA-M (green) ions for simulations with different initial shell velocities $\tilde{V}_{shell} = 1, 5$ and $10\tilde{V}_{thi}$ from top to bottom. These shell values correspond to the cases shown in Figure 3. Results obtained at the y-averaged shock profiles in (a) B_0-OUT and (b) B_0-IN cases.

[32] Figure 10a shows this impact on the percentage of ions suffering the different acceleration mechanisms, where dashed and solid curves correspond respectively to B_0-OUT and B_0-IN configurations. The total percentage (orange) is shown for reference. Present results clearly show that for both B_0 configurations: (1) the density of SDA-NC ions is dominant in particular for low $\tilde{V}_{shell}$ radius but strongly decreases as the ratio $\tilde{V}_{shell}/\tilde{V}_{thi}$ increases (above 2), and becomes comparable to that of SDA-C ions for high $\tilde{V}_{shell}/\tilde{V}_{thi}$ (=10) and for B_0-OUT case; (2) in contrast, the density of DT and of SDA-C ions which is very weak for $\tilde{V}_{shell}/\tilde{V}_{thi}$ radius lower than 4 and 2 respectively, increases with $\tilde{V}_{shell}$ almost simultaneously; (3) in comparison, the increase of SSA is quite moderate and takes place only for $\tilde{V}_{shell}/\tilde{V}_{thi}$ larger than 7.

[33] Some differences appear for B_0-IN configuration with respect to results of B_0-OUT configuration and confirm the expectations mentioned above: (1) the percentage of DT ions strongly increases (almost twice), together with the density of SDA-NC and of SSA ions. These increase take place almost simultaneously provided that $\tilde{V}_{shell}/\tilde{V}_{thi}$ is large enough (>2–3). The increase of SDA-NC percentage is due to their easier interaction with the upstream bump located within the foot area (Figure 1d); (2) the density of SDA-C strongly decreases for $\tilde{V}_{shell}/\tilde{V}_{thi}$ larger than 2. This decrease is due to the difficulties for ions to reach and to overcome the overshoot barrier since some upstream ions may previously interact with the upstream bump (Figure 1d).

[34] Figure 10b shows the impact on the corresponding averaged kinetic energy $\tilde{E}_k$ measured downstream for the different classes of ions. Present results show for B_0-OUT configuration that: (1) the maximum $\tilde{E}_k$ is mainly carried by SDA ions whatever is the $\tilde{V}_{shell}$ value; the value of SDA-C ions dominates that of SDA-NC ions in particular as $\tilde{V}_{shell}/\tilde{V}_{thi}$ is larger than 2; (2) as $\tilde{V}_{shell}/\tilde{V}_{thi}$ increases, the maximum energy gain decreases for SDA-NC ions (red) and increases for SDA-C ions (cyan) so that an increase of $\tilde{V}_{shell}/\tilde{V}_{thi}$ is in favor of

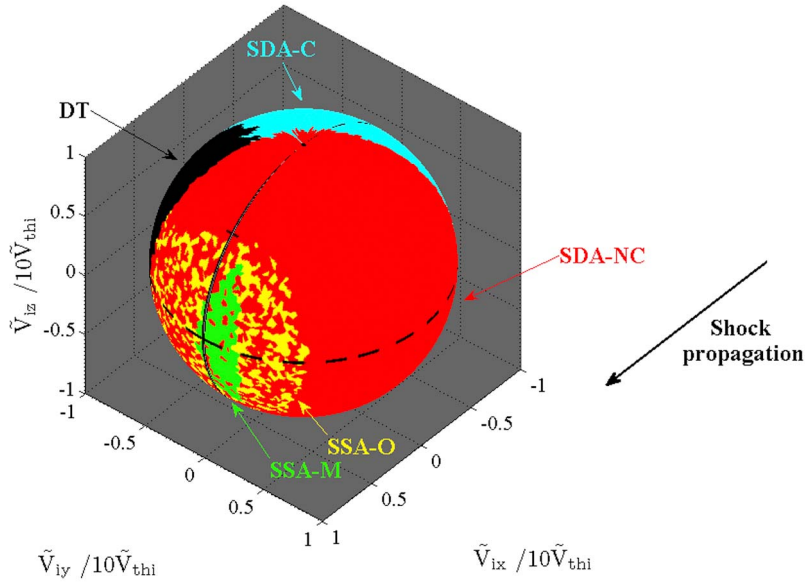

Figure 9. Three-dimensional plot of the angular domain of Figure 8a3 defined for "B_0-OUT" case and $\tilde{V}_{shell} = 10\tilde{V}_{thi}$.

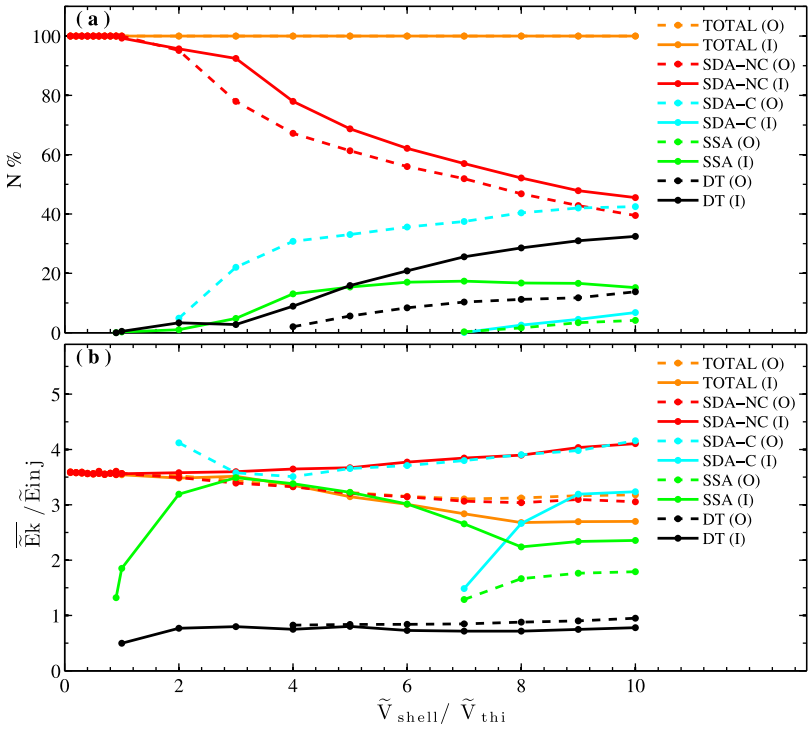

Figure 10. (a) Relative percentage of the different classes of ions measured in downstream region versus the initial shell radius for the "B_0-OUT" (called "O" for short; dashed curves) and "B_0-IN" (called "I" for short; solid curves) configuration and y-averaged shock profiles and (b) corresponding averaged kinetic energy is normalized with respect to the injection kinetic energy $\tilde{E}_{inj} = \tilde{m}_i(M_A\tilde{V}_A)^2/2$. This figure represents the averaged kinetic energy (e.g., $\bar{\tilde{E}}_{k\ total} = \frac{\sum_{SDA-C}\tilde{E}_k + \sum_{SDA-NC}\tilde{E}_k + \sum_{SSA}\tilde{E}_k + \sum_{DT}\tilde{E}_k}{N_{SDA-C} + N_{SDA-NC} + N_{SSA} + N_{DT}}$, where $\bar{\tilde{E}}_{k\ SDA-C} = \frac{\sum_{SDA-C}\tilde{E}_k}{N_{SDA-C}}$, $\bar{\tilde{E}}_{k\ SDA-NC} = \frac{\sum_{SDA-NC}\tilde{E}_k}{N_{SDA-NC}}$ etc.) and not the total kinetic energy.

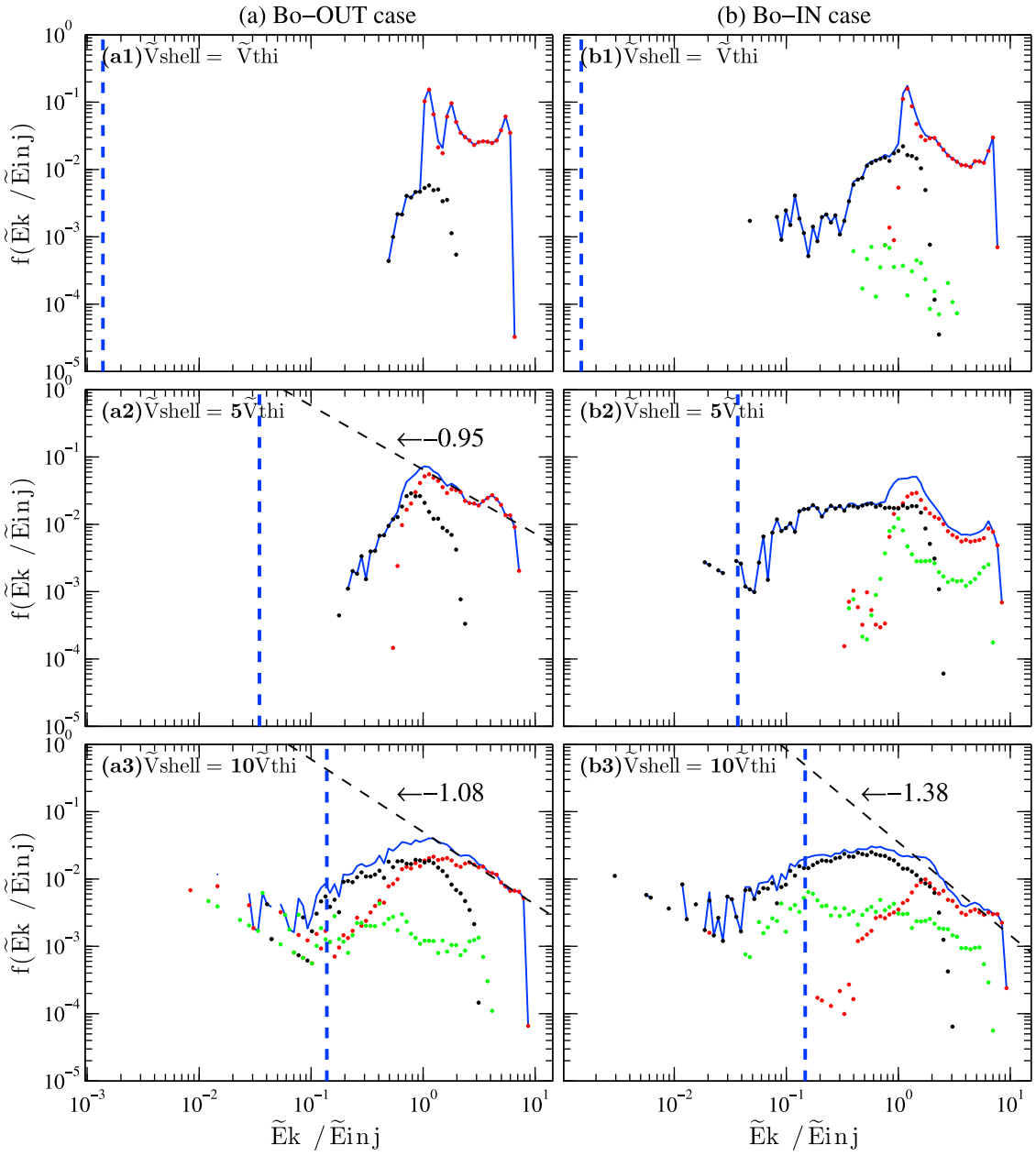

Figure 11. Downstream energy spectra of ions measured in the simulation frame (i.e., upstream frame) corresponding to the cases shown in Figure 3. Red, green, and black dots indicate the contributions of "SDA", "SSA" and "DT" ions to the total spectra (blue solid curve), respectively. For reference, the vertical arrow indicates the initial injection kinetic energy $\tilde{E}_{inj} = \tilde{m}_i\left(M_A\tilde{V}_A\right)^2/2$, defined at time $\tilde{t} = 0$.

SDA-C ions both in terms of percentage and averaged kinetic energy; more SDA-C are formed with higher initial energy; (3) the averaged energy gain stays almost constant for DT ions. This means that, as $\tilde{V}_{shell}/\tilde{V}_{thi}$ increases, more DT ions are produced (Figure 10a) but these do not gain more energy.

[35] The results obtained for B_0-IN configuration can be summarized as follows: (1) the averaged energy gain strongly decreases for SDA-C ions, and increases for SDA-NC and SSA ions; (2) almost no change is observed for DT ions. Let us precise that Figure 10b represents the averaged kinetic energy and not the total kinetic energy which is expected to increase in B_0-IN configuration where the density of DT ions strongly increases.

[36] Downstream energy spectra of ions are shown in Figure 11 for the cases analyzed in Figures 3a and 3b. These spectra are measured from the ramp to far downstream ($\tilde{X}_{ramp} - 10\tilde{c}/\tilde{\omega}_{pi}$) in the simulation frame (i.e., upstream frame). Contributions of various particle classes (namely SDA, SSA and DT) are color-coded separately by red, green and black. The total spectrum (all mixed populations) are represented by a blue solid curve. For B_0-OUT case, results are similar to those obtained with a 1-D simulation by *Yang*

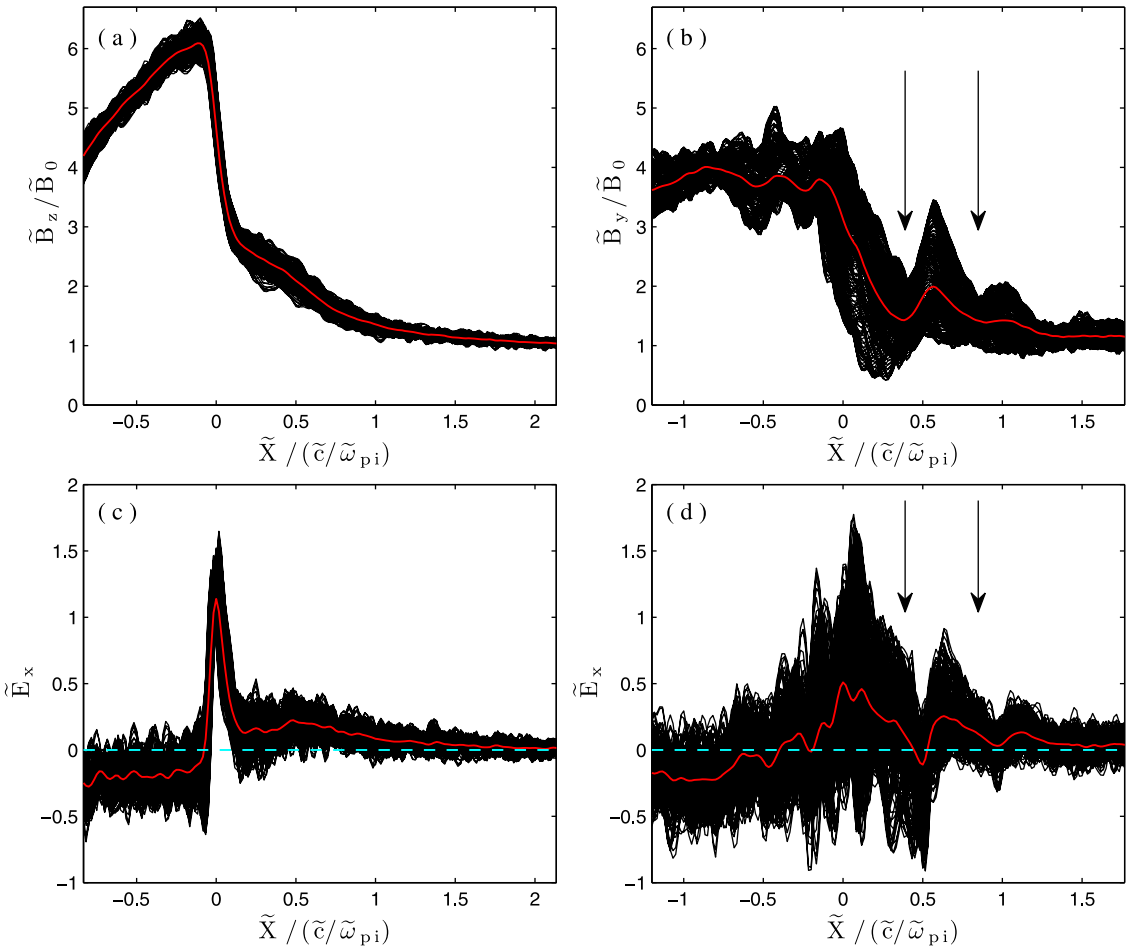

Figure 12. Profiles of the main magnetic field and of the electrostatic field $\tilde{E}_x$ for the (a and c) "B_0-OUT" and (b and d) "B_0-IN" configurations. In each panel, the different x-profiles measured for all y-values are superimposed; the corresponding y-averaged profile (red) is indicated too. The ramp location is used as the origin $\tilde{x} = 0$ of the plot.

et al. [2009a] and are summarized as follows: (1) high energy part of the spectra is always dominated by SDA ions no matter how large $\tilde{V}_{shell}$ is; (2) the variation of $\tilde{V}_{shell}$ has a filtering effect in such a way that the SSA population contributes more noticeably to the total energy spectrum as $\tilde{V}_{shell}$ increases; simultaneously, the energy range of each population enlarges too; (3) for large shell cases, the middle part ($1.1 < \tilde{E}_k/\tilde{E}_{inj} < 8$) of the total energy spectrum forms a power law (here the index is 1.08 in Figure 11a3); this power law is mainly supported by both DT and SDA ions which contribute. No power law can be defined for low $\tilde{V}_{shell}/\tilde{V}_{thi}$ ration (Figure 11a1).

[37] A few differences appear in the B_0-IN configuration (Figure 11b) with lower fields gradient at the shock front: (1) for low and middle $\tilde{V}_{shell}/\tilde{V}_{thi}$ values, the energy spectrum is more extended in particular to lower energy values. This extension is mainly supported by DT ions which succeed to pass (with lower energy) through the lower amplitude shock front (Figure 11b2). In short, the effect of low fields gradient at the shock front has strong impact; (2) for high $\tilde{V}_{shell}/\tilde{V}_{thi}$ value, the differences in spectra are weaker with respect to B_0-OUT configuration (Figures 11b3 and 11a3); the effect of varying $\tilde{V}_{shell}$ has a stronger impact. In this case, the only noticeable impact (in particular, of low fields gradient at the shock front) is on the power law index which increases from 1.08 to 1.38.

3.2. Impact of Shock Front Ripples on the Dynamics of Ions for B_0-OUT and B_0-IN Configurations

[38] In this section, we follow a similar procedure as in section 3.1 but by using the shock profile directly issued from 2-D PIC simulation in B_0-IN case, i.e., without any y-averaging. Let us remind shortly the essential differences between shock profiles in B_0-OUT case and B_0-IN (Figure 12): first, for y-averaged profiles, the fields amplitude at the shock front is lower, the thickness of the front itself (in particular of the ramp) is larger in B_0-IN (Figures 12b and 12d) than in B_0-OUT (Figures 12a and 12c) configuration, and the fields of the shock profile do not follow a monotonic variation from upstream to the ramp. Second, for non-averaged profile, the scale of the shock front ripples is much larger in B_0-IN (Figures 12b and 12d) as compared to B_0-OUT case (Figures 12a and 12c). The impact of these ripples is the main

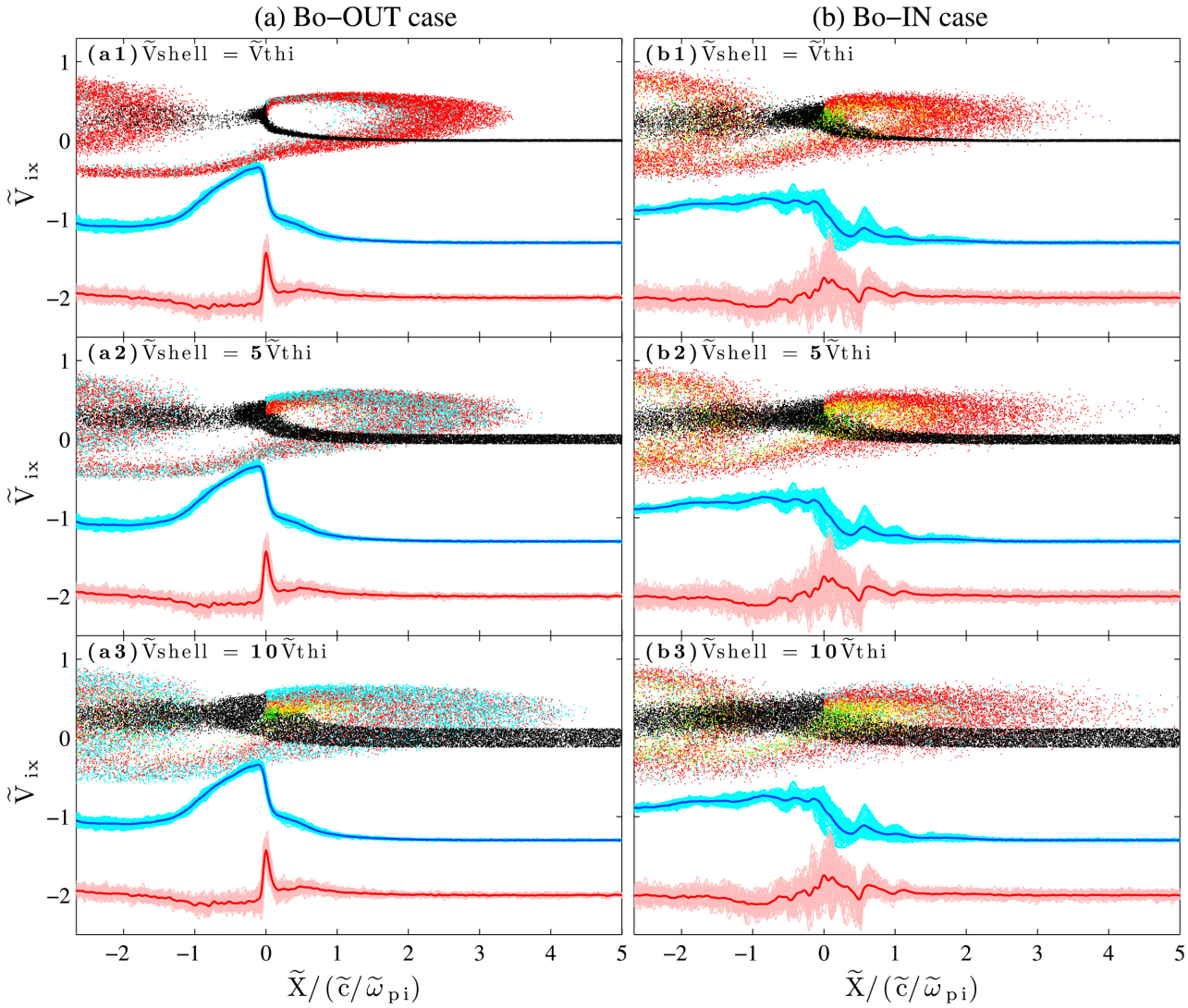

Figure 13. Ion phase space ($\tilde{V}_{ix}$-$\tilde{X}$) of ions issued from 2-D test particles simulations for three different initial shell velocities $\tilde{V}_{shell}$ = 1, 5 and 10$\tilde{V}_{thi}$ for the non-averaged shock profiles (i.e., front rippling included). Results are shown respectively for (a) "B_0-OUT" and (b) "B_0-IN" configurations. Spatial coordinate is normalized versus the ion inertial length $\tilde{c}/\tilde{\omega}_{pi}$. The ramp location is used as the origin $\tilde{x} = 0$ of the plot. Colors code is as follows: incoming and DT ions (black), SDA-C ions (cyan), SDA-NC ions (red), SSA-O ions (yellow) and SSA-M ions (green). For reference, the non-averaged fields of the shock profile $\tilde{B}_z$ (cyan) and $\tilde{E}_x$ (magenta) (as in Figure 12) are shown in each panel. The corresponding y-averaged fields $\tilde{B}_z$ (blue) and $\tilde{E}_x$ (red) are also shown for reference as in Figure 3.

center of interest herein. However, two additional features need to be noted: (1) the amplitude of the electric field fluctuations at the ramp in Figure 12d is so large that it can be comparable to (or even slightly larger than) the amplitude of the same field in Figure 12c (local y-averaged and non-averaged field measured in the ramp); so this feature can have a particular impact on ions surfing at the ramp (such as SSA-M ions) and on ions crossing the ramp (such SDA-C ions) both types being already identified in subsection 3.1; (2) for B_0-IN configuration, the amplitude of the noticeable bump observed before the ramp (in the spatial domain identified between vertical arrows) can be strongly amplified by the rippling (Figures 12b and 12d). These local fluctuations have a particular impact on ions which mainly interact with the so called "foot" region of the shock (such as SSA-O and SDA-NC ions also identified in subsection 3.1) and do not reach the ramp. One question emerges: do we still observe the different groups of ions in presence of different size ripples?

[39] Figure 13 shows the ion phase space plots for different shell velocity distributions. The ions suffering different acceleration mechanisms are marked by different colors as in Figure 3. The main differences between Figures 13 and 3 are summarized as follows.

[40] 1. As expected, the ions are more diffuse in phase space in the presence of shock front rippling (Figure 13) whatever are the $\tilde{V}_{shell}$ value and the B_0 configuration.

[41] 2. The diffusion of reflected and DT ions by large scale ripples (Figure 13b1) is much more important than that due to small scale ripples (Figure 13a1) whatever the $\tilde{V}_{shell}$ value is.

As a particular consequence, for low energy cases, no coherent vortex can persist in the reflected ions motion (Figure 13b1) as compared with the y-averaged case (Figure 3b1); the coherent gyrating motion of reflected ions is destroyed by the front rippling.

[42] 3. In addition, the front ripples (Figures 13a and 13b) increase the upstream extension of the reflected ions as compared with y-averaged case (Figures 3a and 3b). This upstream extension is moderate for small scale rippling (Figure 13a versus Figure 3a), but much larger for large scale rippling (Figure 13b versus Figure 3b). Let us remind that two effects combine together; on one hand, for B_0-IN configuration, a lower ion reflection due to lower fields amplitude at the front (Figure 3b) but higher ion diffusion due to the large scale rippling (Figure 13b); on the other hand, the situation is reversed for the B_0-OUT configuration, with a stronger coherent ion reflection due to a higher fields amplitude at the front which leads to a larger upstream extension (Figure 3a versus Figure 3b) but with a lower ion diffusion due to the small scale rippling (Figure 13a versus Figure 13b). Finally, with non-averaged cases, the upstream extension of reflected ions is slightly larger for large rather than for small scale rippling cases; this reflected ions domain measured from the locations of the respective ramps are $\tilde{\Delta}_{ref,ions} = 3.4$ versus 3.85, 3.8 versus 4.4, and 4.5 versus 4.8 $\tilde{c}/\tilde{\omega}_{pi}$ respectively for $\tilde{V}_{shell}/\tilde{V}_{thi} = 1$ (Figures 13a1 and 13b1), 5 (Figures 13a2 and 13b2) and 10 (Figures 13a3 and 13b3) for small versus large scale rippling.

[43] 4. For low $\tilde{V}_{shell}$ case, DT ions which are absent in the y-averaged case of B_0-OUT configuration (i.e., all ions are reflected in Figure 3a1) now emerge in the corresponding non-averaged case (Figure 13a1); in other words, the front rippling facilitates the formation of DT ions. The production of DT ions is even larger for large scale ripples (Figure 13b1 versus Figure 13a1). In both B_0 configurations, the shock front (which can be considered as playing the role of an electric and magnetic barrier for ions) becomes "more porous" in the presence of rippling.

[44] 5. For low $\tilde{V}_{shell}$ case, both SSA-M (green) and SSA-O (yellow) ions which were almost absent in the y-averaged case of B_0-IN configuration (Figure 3b1), now emerge in the corresponding non-averaged case (Figure 13b1). This feature which will be even more evidenced in the angular domains of Figure 15, implies that large scale ripples largely help the formation of SSA ions.

[45] 6. For low $\tilde{V}_{shell}$ case and for B_0-OUT configuration, small scale ripples help the formation of SDA-C ions (cyan) as seen Figure 13a1, which were absent in y-averaged case (Figure 3a1).

[46] All main features of the four reflected ion populations (as identified in Figure 4 for y-averaged profiles) have been fully recovered in the presence of front rippling (not shown here). However, a major point is that a given ion (i.e., belonging to given group) identified for y-averaged case belongs to a different group when considering the same ion for non-averaged case. There is no one-to-one correspondence of ions when analyzing y-averaged and non-averaged cases. Moreover, a statistical study made on 2-D shock profiles (not shown here) confirms that SDA ions always get an energy gain much larger than the SSA ions for both B_0-OUT configuration (Figures 4a5–4a8) and B_0-IN (Figures 4b5–4b8) shock profiles. This extends to 2-D results a fact which has been observed for 1-D shock profile in recent work [*Yang et al.*, 2009a]. The SSA process reveals not to be the dominant process.

[47] The impact of the front ripples is illustrated in Figures 14a and 14b which shows the trajectory analysis and the averaged kinetic energy of a few SSA ions for shell velocity distributions radius $\tilde{V}_{shell} = 10\tilde{V}_{thi}$. The ions suffering SSA-O and SSA-M are color-coded by different colors as in Figure 5. These SSA ions are selected among the 51200 ions used in the simulations as in Figure 5. The main differences with respect to results of y-averaged shock profiles are as follows:

[48] 1. For both B_0 configurations, in the presence of front ripples, the trajectories of SSA ions become more diffuse since these interact with local fields of different amplitudes (at different y-locations as illustrated in Figure 12) but the final energy gain is almost unchanged with respect to y-averaged case at least for small scale rippling (Figure 14a). This diffusion leads to some temporal "chaotic" evolution of local kinetic energy (partial loss of the reflected ion motion coherency) as ions receive a small kick up or down due to the front rippling itself (Figures 14a and 14b). This "chaotic" feature is reinforced for large scale rippling (Figures 14b3 and 14b4) as compared to small scale rippling (Figures 14a3 and 14a4); as a consequence, in the B_0-IN configuration, the resulting energy gain is higher (Figures 14b3 and 14b4) than for the corresponding y-averaged shock profiles (Figures 5b3 and 5b4).

[49] 2. For both B_0 configurations, the front rippling leads to a mixing of injection angle domains for the SSA-O ions and SSA-M ions (i.e., ions change categories), and enlarges these angular domains. This domain extension is much larger for large scale rippling (Figure 14b5 to be compared with Figure 5b5) rather than for small scale rippling (Figure 14a5 to be compared with Figure 5a5).

[50] 3. For non-averaged case of B_0-IN configuration, the large scale ripples lead to an increased kinetic energy for both classes of SSA ions (Figures 14b3 and 14b4) as compared with y-averaged cases (Figures 5b3 and 5b4). This increase is even much stronger for SSA-M (Figure 14b4) in association with the stronger ion diffusion by large scale ripples. Then, even in this B_0-IN configuration, where the y-averaged fields amplitude at the shock front is lower (Figures 12b and 12d) than that for B_0-OUT (Figures 12a and 12c), the large scale rippling allow some SSA ions to reach an energy gain higher (Figures 14b3 and 14b4) than that for B_0-OUT (Figures 14a3 and 14a4). This feature can be explained by the fact that SSA-M ions interact mainly near or at the ramp i.e., where the gradient of $\tilde{E}_x$ (whose large amplitude is determinant to initiate SSA-M ion) is the largest. Moreover, in the present case, the fluctuations of the electric field at or near the ramp are very large so that the amplitude of the local electric field for a given y-location (Figure 12d) can overcome that observed at the ramp for B_0-OUT configuration (Figure 12c), and the resulting energy of an SSA-M ion interacting at that y-location can be higher. Similarly, the fluctuations of the local electric field are also quite large at/around the upstream bump (between arrows in Figure 12d) and represent an important percentage of the

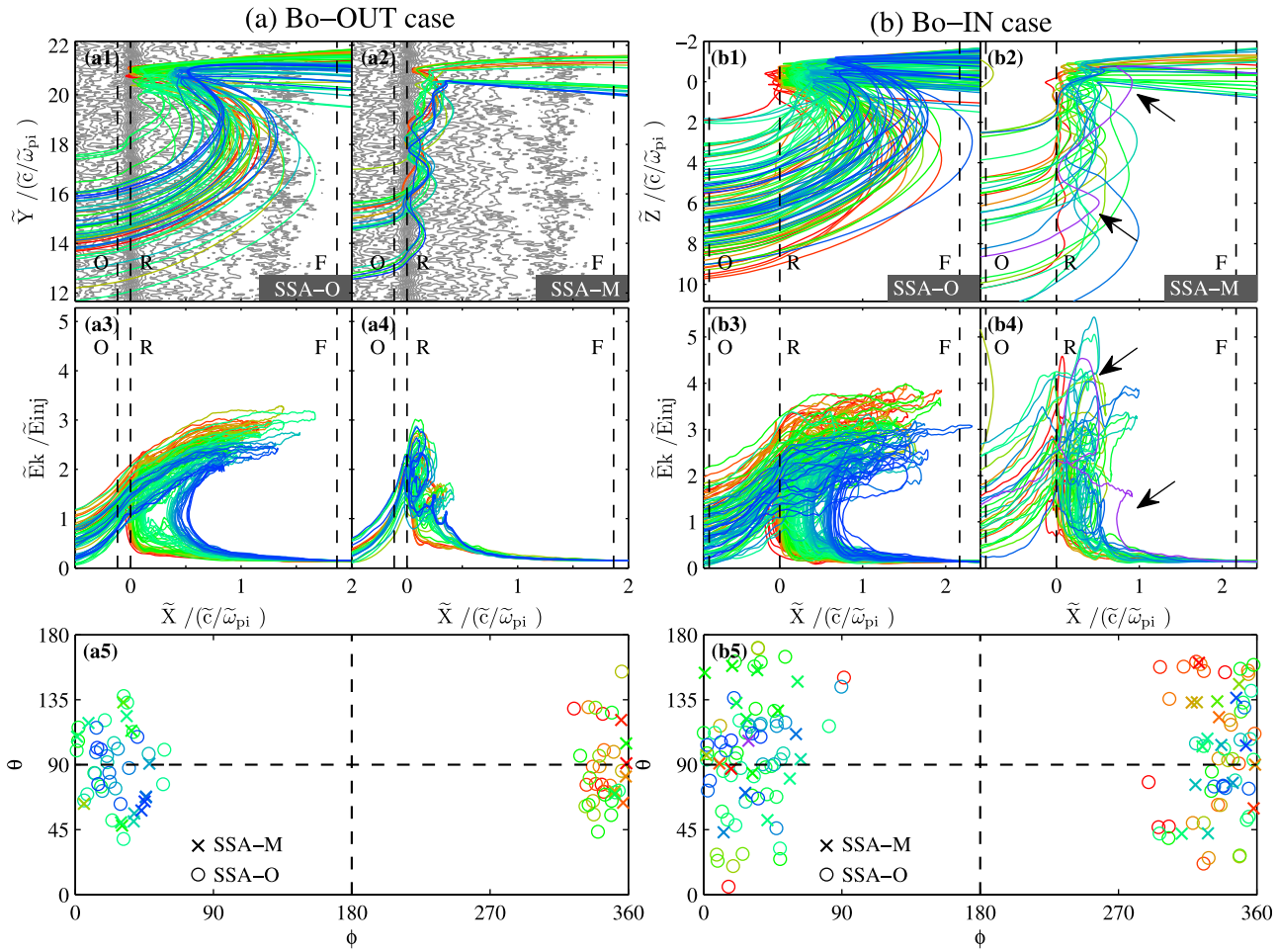

Figure 14. (a) Plots similar to those of Figure 5, focused on different reflected ions (different colors) suffering SSA-O (Figure 14a1) and SSA-M (Figure 14a2) processes for the non-averaged "B_0-OUT" configuration and for $\tilde{V}_{shell} = 10\tilde{V}_{thi}$. Vertical thick dashed lines from left to right indicate the locations of the overshoot "O", the ramp "R" and the upstream edge of the foot "F" respectively. Figures 14a3 and 14a4 show the corresponding normalized kinetic energy $\tilde{E}_k/\tilde{E}_{inj}$ versus $\tilde{X}/(\tilde{c}/\tilde{\omega}_{pi})$, where the injection kinetic energy $\tilde{E}_{inj} = \tilde{m}_i(M_A\tilde{V}_A)^2/2$.The ramp location is used as the origin $\tilde{x} = 0$ of the plot. Figure 14a5 shows the domain of velocity injection angles $(\theta - \phi)$ of SSA-O (circle) and SSA-M (cross) ions. (b) Similar plots for the non-averaged "B_0-IN" configuration.

same field at the ramp. This feature explains the increase in the percentage and in the averaged kinetic energy of SSA-M ions. As an illustration, an ion (purple) identified by two arrows in Figures 14b2 and 14b4 (at different times of its trajectory) is characterized by a high energy gain before the ramp; its turning point is located at a distance $\tilde{x} = 0.65\,\tilde{c}/\tilde{\omega}_{pi}$ upstream from the ramp which corresponds exactly to the location of the upstream bump extending within the range $\tilde{x} = 0.37 - 0.87\,\tilde{c}/\tilde{\omega}_{pi}$ from the ramp (Figures 12b and 12d). Let us remind that partial statistics are considered at that stage and only a few particles can get so high energy gain; the full statistics analysis based on all injected ions is necessary and is presented in Figures 15–17, in order to establish conclusive statements.

[51] 4. For B_0-IN case, the number of reflections of SSA-M ions and the associated kinetic energy largely increases (Figures 14b2 and 14b4) with respect to the y-averaged case (Figures 5b2 and 5b4). The invoked reason is indicated in above point 3.

[52] Figure 15 shows the complete statistical results of the injection angles domains for SSA-O (yellow), SSA-M (green), SDA-C (cyan), SDA-NC (red), and DT (black) ions for B_0-IN case. The main features are summarized as follows:

[53] 1. One main result is that whatever are the shell radius and the B_0 configuration, the front rippling "blurs" out the frontiers well identified between the different classes of ions in all y-averaged cases (Figure 8). The injection angle domains of the different populations expand and interpenetrate one each other. A separate analysis (not shown herein) evidences that one ion belonging to a category in y-averaged case can change category in non-averaged case; there is no one-to-one correspondence. In other words, the front rippling makes the shock front "porous" as illustrated by comparing Figures 15 and 8; this "porosity" (or diffusion of ions at the frontiers of their angular domains) is much larger for large scale (Figure 15b) rather than for small scale rippling (Figure 15a).

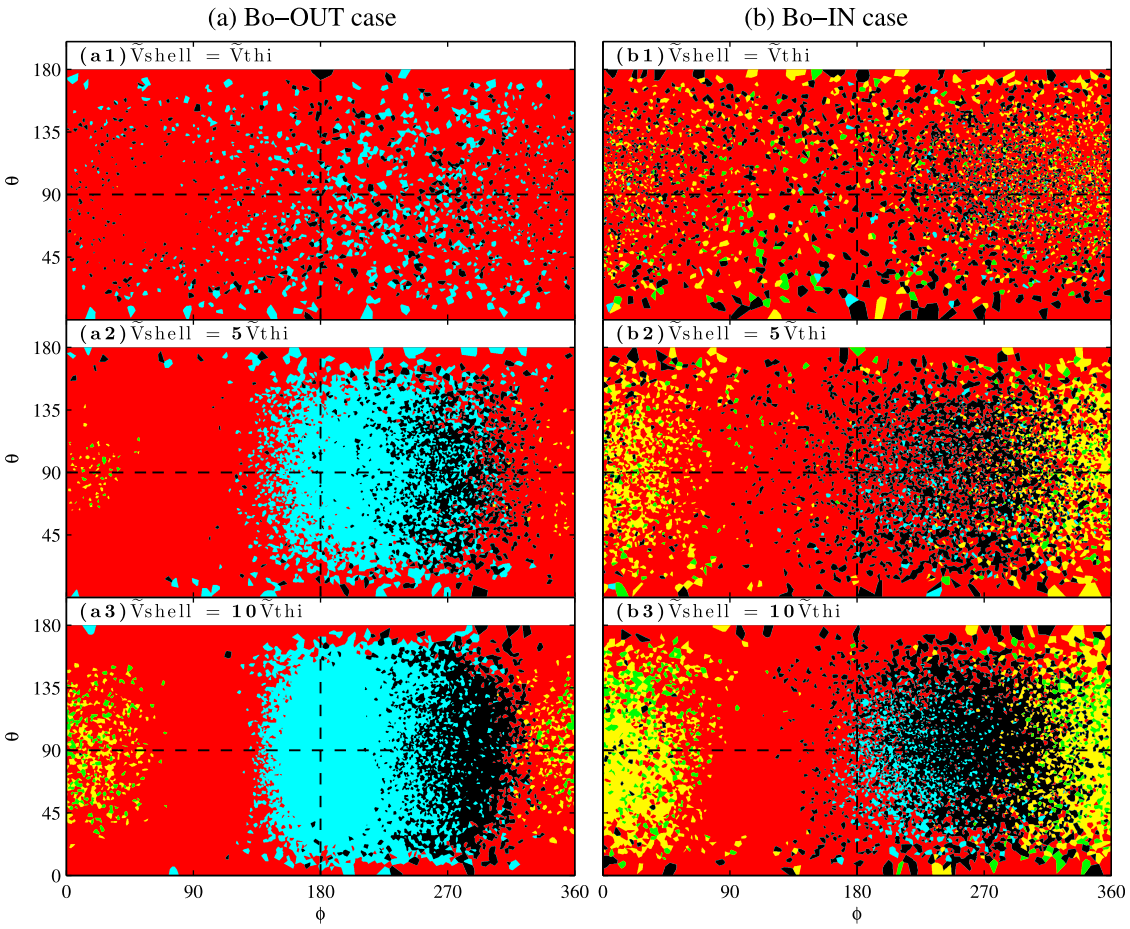

Figure 15. Domain of velocity injection angle ($\theta - \phi$) for DT (black), SDA-C (cyan) SDA-NC (red), SSA-O (yellow) and SSA-M (green) ions for simulations with different initial shell velocities $\tilde{V}_{shell} = 1, 5$ and $10\tilde{V}_{thi}$ from top to bottom. These shell values correspond to the cases shown in Figure 13. Results obtained at the non-averaged shock profiles for (a) "B_0-OUT" and (b) "B_0-IN" configurations.

[54] 2. For small $\tilde{V}_{shell}$ case (Figure 15a1), the rippling facilitates the formation of DT and SDA-C ions as announced when analyzing Figure 12a1. Again, if one considers the shock front as a magnetic and an electrostatic barrier for ions, the front rippling makes this barrier "porous" in the sense that DT ions can be transmitted more easily, and some reflected ions may have their turning point behind the overshoot and are identified as new SDA-C ions.

[55] 3. For the B_0-OUT configuration and for the middle $\tilde{V}_{shell}$ case (Figure 15a2), both SSA-O and SSA-M ions obviously emerge within angular ranges ($0° < \phi < 340°$ and $320° < \phi < 360°$) centered around $\theta = 90°$, while these are absent in y-averaged case (Figure 8a2). As $\tilde{V}_{shell}/\tilde{V}_{thi}$ increases, the frontier between angular domains of SSA-O (yellow) and SSA-M (green) observed in the y-averaged case (Figure 8a3) almost disappears in the presence of small scale rippling (Figure 15a3); their angular domain largely expands from $45° < \theta < 135°$ to roughly $25° < \theta < 155°$ (Figure 15a3). In other words, SSA-ions are more easily evidenced in presence of front rippling (provided that the shell radius is large enough), but the rippling itself mixes the injection angle domains of both SSA-O and SSA-M populations.

[56] Solid curves in Figure 16 indicate statistical results of the different classes of ions identified in the downstream region at the end of the simulations and are compared with results of y-averaged cases in Figure 10; same statistical procedure and same colors code are used for identifying the different ion populations in both Figures 16 and 10. Main results are:

[57] 1. For both B_0 configurations, the front rippling is confirmed as being a good candidate to facilitate the formation of DT (black), SSA (green) ions and improves slightly the formation of SDA-C (cyan) ions. It is important to note that all these variations take place mainly within low and middle $\tilde{V}_{shell}/\tilde{V}_{thi}$ values ranges, and are particularly strong for large scale rippling (solid curves) rather than for small scale (dashed curve) rippling. All results obtained for high $\tilde{V}_{shell}/\tilde{V}_{thi}$ (=10) are almost unchanged with respect to y-averaged case.

[58] 2. For both B_0 configurations, the front rippling is not in favor of the formation of SDA-NC ions. More precisely, the large scale rippling (solid curves) lead to a strong decrease of the SDA-NC (red) ions percentage (within the range $\tilde{V}_{shell} < 8\tilde{V}_{thi}$), while the percentage of DT and SSA ions increases within the ranges $\tilde{V}_{shell} < 6.8\tilde{V}_{thi}$ and

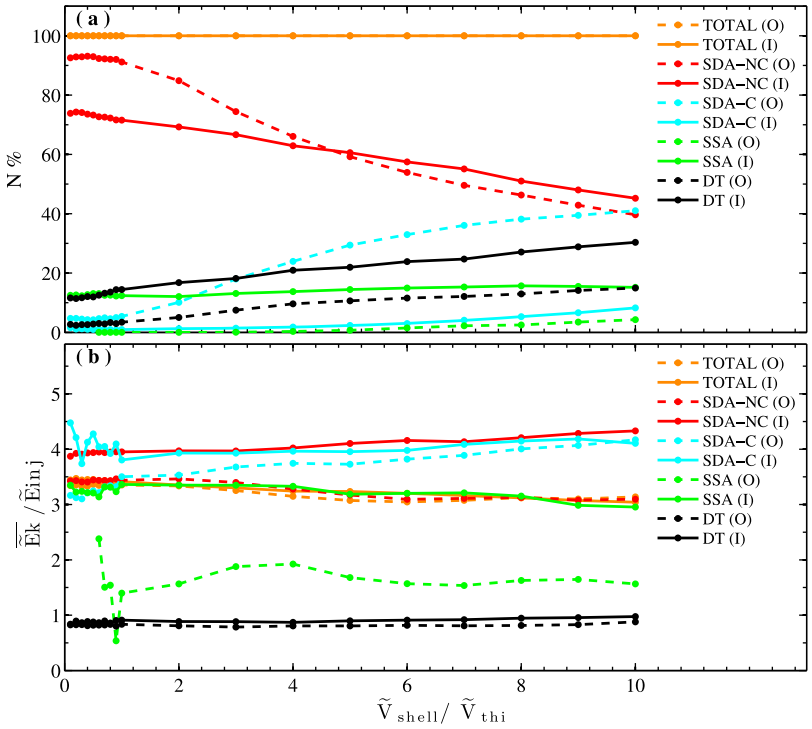

Figure 16. (a) Relative percentage of different classes of ions measured in the downstream region versus the initial shell radius for the "B_0-OUT" (called "O" for short; dashed curves) and "B_0-IN" (called "I" for short; solid curves) configuration and non-averaged shock profiles and (b) corresponding averaged kinetic energy normalized with respect to the injection kinetic energy $\tilde{E}_{inj} = \tilde{m}_i \left(M_A \tilde{V}_A\right)^2 / 2$.

$\tilde{V}_{shell} < 4\tilde{V}_{thi}$ respectively as compared with y-averaged case (Figure 10a).

[59] 3. For all populations, the rippling contributes to provide a noticeable value of the averaged kinetic energy for ion populations which succeed to emerge (DT, SSA, and SDA-C ions) as compared with y-averaged case where their kinetic energy was null or negligible. This major change takes place within the low and middle $\tilde{V}_{shell}/\tilde{V}_{thi}$ values range, but is rather more limited for high $\tilde{V}_{shell}/\tilde{V}_{thi}$ (=10) value. For both small and large scale rippling, the resulting averaged kinetic energy has a limited dependance versus the $\tilde{V}_{shell}/\tilde{V}_{thi}$ ratio (Figure 16b).

[60] 4. In short, the amplitude of fields fluctuations along the shock front is much larger for B_0-IN than for B_0-OUT configurations (Figure 12) and contributes to change strongly the relative distribution of the upstream ions into the different classes. The resulting particles diffusion strongly increases for all ion classes (both in terms of injection angles as in Figures 15a and 15b, and in the phase space as in Figures 13a and 13b), but the impact of the large scale ripples on the averaged kinetic energy is only noticeable in low and middle $\tilde{V}_{shell}/\tilde{V}_{thi}$ values range, with respect to the y-averaged case (Figure 16b).

[61] Finally, downstream ion energy spectra are shown in Figure 17 for both "B_0-OUT" and "B_0-IN" configurations and are compared with those of Figure 11. The main differences are as follows:

[62] 1. For both B_0 configurations and for low/middle $\tilde{V}_{shell}/\tilde{V}_{thi}$ values (Figures 17a1, 17b1, 17a2, and 17b2), the contribution of DT, SSA and SDA ion populations to the total spectrum increases in presence of front rippling with respect to the y-averaged case (Figures 11a1, 11b1, 11a2, and 11b2). In particular, the contribution of SSA and SDA ions to the low and middle energy part of the total spectrum is enhanced. Indeed, more lower energy ions are identified as SSA and SDA when interacting with the fluctuations of the bump upstream of the ramp; on the same, more lower energy DT ions succeed to pass through the lower amplitude fluctuating overshoot at the front. This enhancement is stronger for large scale ripples (Figures 17b1 and 17b2) rather than for small scale ripples (Figures 17a1 and 17a2). As a consequence, the front rippling strongly enlarges the spectrum range toward lower energy $\tilde{E}_k/\tilde{E}_{inj}$ for each DT, SSA and SDA population; the energy range of the resulting total spectrum enlarges too.

[63] 2. In contrast, whatever is the ripples size, the impact of the front rippling is quite moderate for high $\tilde{V}_{shell}/\tilde{V}_{thi}$ (=10) value (Figures 17a3 and 17b3) with respect to the y-averaged case (Figures 11a3 and 11b3). One important point is that the resulting power law evidenced for large shell radius still persists and is not affected by the front rippling: within the same middle energy range, the index is still 1.08 in Figures 11a3 and 17a3, and 1.38 in Figures 11b3 and 17b3. Let us note that a lower gradient of shock front is in favor for increasing the power index (1.08 to 1.38 between Figures 11a3 and 11b3). Moreover, present results show that, even in the presence of different scales of the front ripples, this power law is not determined by SSA-M ions (equivalent of MRI ions as suggested by *Zank et al.* [1996]) but rather a by strong contribution of SDA and DT ions. This difference could be explained

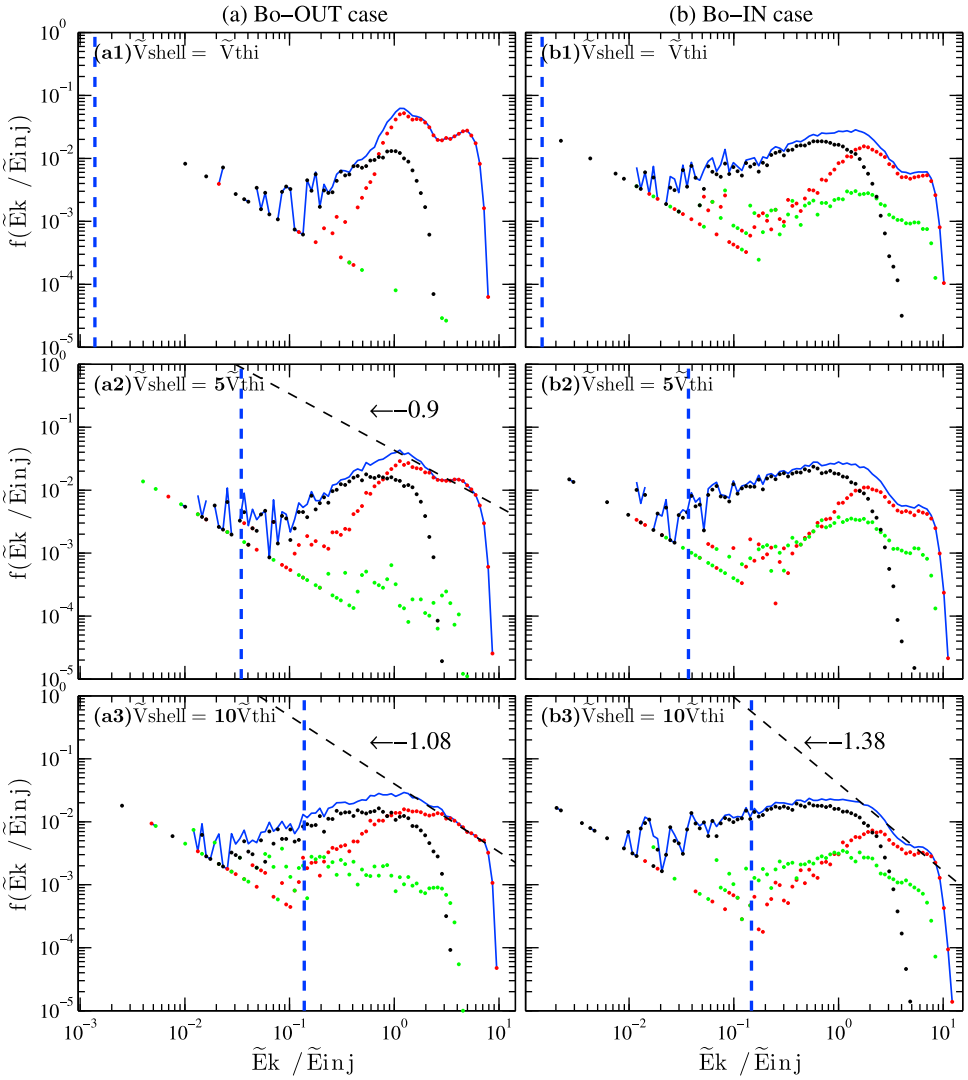

Figure 17. Downstream energy spectra of ions measured in the simulation frame (i.e., upstream frame) corresponding to the cases shown in Figure 13. Red, green, and black dots indicate the contributions of "SDA", "SSA" and "DT" ions to the total spectra (blue solid curve), respectively. For reference, the vertical arrow indicates the initial injection kinetic energy $\tilde{E}_{inj} = \tilde{m}_i \left(M_A \tilde{V}_A\right)^2/2$, defined at time $\tilde{t} = 0$.

by the fact that the model of *Zank et al.* [1996] is based on several simplifying assumptions (in particular concerning the microstructures of the shock included herein), and a one-to-one corresponding comparison cannot be directly achieved.

[64] 3. For both B_0 configurations, the maximum energy of the total spectrum is still carried by SDA ions for any $\tilde{V}_{shell}/\tilde{V}_{thi}$ value; this maximum slightly increases in the presence of ripples. The SSA process is not dominant in any case; this extends to 2-D shock profiles a previous result obtained for 1-D simulation [*Yang et al.*, 2011a].

4. Conclusions

[65] In this paper, we use electromagnetic fields of a strictly perpendicular shock produced self-consistently in 2-D PIC simulations, and test-particle simulations in order to analyze the dynamics and energization of upstream ions interacting with rippled shock fronts. Three types of analysis are presented: first, a parametric analysis has been performed by varying initial kinetic energy of the shell distribution ions; second, this analysis has been applied on two different types of rippled shock front so-called respectively "B_0-OUT case" (equivalent to the shock profile issued from a 2-D PIC simulation when the ambient magnetic field $\tilde{B}_0$ is perpendicular to the simulation plane) and "B_0-IN case" (equivalent to the shock profile issued from a 2-D PIC simulation when $\tilde{B}_0$ is lying within the simulation plane). The first and second cases are characterized respectively by a small scale front rippling (with a wavelength along the shock front less than 1 $\tilde{c}/\tilde{\omega}_{pi}$) and a large scale front rippling (with a wavelength along the shock front covering one or a few $\tilde{c}/\tilde{\omega}_{pi}$). Third, for each case, the investigation is based on systematic comparison between y-averaged and non-averaged (i.e., originally rippled) shock profile. Y-averaged profile of "B_0-IN" case is characterized by smoother gradient of the fields at the shock front (smaller shock amplitude, and a thicker shock front, and in particular thicker ramp) as compared to the "B_0-OUT" case. Main results can be summarized as follows:

[66] 1. Three different ion populations can be identified (SDA, SSA and DT) after upstream ions have interacted with the shock front as in recent 1-D simulations made by *Yang et al.* [2009a]. In addition, the SSA ions are divided into two subpopulations: SSA-O and SSA-M ions according to their respective number of bounces. As in 1-D simulation, SSA-O ions can reach a high energy during one bounce only. Their acceleration mechanism is different from that of the SSA-M ions; they are reflected not only at the ramp, but also within the foot where these suffer a strong acceleration. This feature is not supported by any current theory yet. In contrast, the behavior of the SSA-M ions is as expected by previous theoretical analysis [*Shapiro and Üçer*, 2003]; however, it can be initiated also within the foot region so before the ions reach the ramp itself. Furthermore, a y-averaged (thicker) shock front as obtained in "B_0-IN" case helps the formation of SSA-O as compared to the "B_0-OUT" case (thinner shock front). This means that a very thin ramp is not a necessary condition to initiate the SSA process. Instead, we consider rather that an $\tilde{E}_x$ field strong enough is a condition to initiate the SSA process even at the foot. At least, for non-averaged shock profile, large scale front ripples ("B_0-IN" case) increase the percentage and the downstream average kinetic energy of SSA ions especially for small and large ratio $\tilde{V}_{shell}/\tilde{V}_{thi}$ (less than 4 and larger than 6 respectively), while small scale front ripples have a weaker impact on SSA ions.

[67] 2. Moreover, the SDA ions are divided into two subpopulations: SDA-C and SDA-NC. For the y-averaged shock front, the profiles of "B_0-IN" case tend to increase the formation of SDA-NC ions and to decrease strongly SDA-C ions percentage as compared to the "B_0-OUT" case. For non-averaged shock profiles, the percentage of SDA-NC is more strongly decreased by large scale front ripples as compared to the small scale front ripples. However, large scale front ripples slightly increase the averaged kinetic energy of SDA-NC ions, which suggests that if less SDA-NC ions are produced these are more energetic. Correspondingly, small scale ripples have a weak effect on the averaged kinetic energy of SDA-NC ions.

[68] 3. Y-averaged profiles of "B_0-IN" case greatly help the formation of DT ions, which can be easily explained by the lower amplitude of the shock front. However, no noticeable change is observed in the averaged kinetic energy between y-averaged and non-averaged shock profiles, for any value of $\tilde{V}_{shell}/\tilde{V}_{thi}$ larger than 2, for each "B_0-IN" and "B_0-OUT" configuration. This suggests that if more DT ions are produced these are not more energetic.

[69] 4. It is worth noting that the shock front ripples do have a strong impact on the injection angles, on the percentage and the resulting energy spectrum of upstream ions after these interact with the shock front, except for large $\tilde{V}_{shell}/\tilde{V}_{thi}$ (=10). These main impacts are: (1) because of the presence of ripples, local electric and magnetic fields interacting with ions at different y-locations along the shock front are quite different; as a consequence, more SSA and DT ions are formed; (2) a diffusion of ions takes place at the frontiers of the injection angle domains and in the phase space, in such a way that the different classes of ions are mixed and their respective angular domains expand and interpenetrate one to each other. Then, the frontiers between the different angular domains clearly defined for each ion population for y-averaged case are blurred out when the front ripples are included; in other words, the shock front becomes "porous".

[70] 5. In all $\tilde{V}_{shell}$ cases, SDA ions are always dominant in the high energy range part of the downstream energy spectrum, in the relative percentage as well as in downstream averaged kinetic energy (independently of the SDA-C or SDA-NC class). The front rippling maintains this dominance and even reinforces it for low $\tilde{V}_{shell}/\tilde{V}_{thi}$ ratio values.

[71] In this paper, we have focused our attention on the impact of a self-consistent shock front rippling (with different spatial scales along the front) on the dynamics of ions for the most simple configuration i.e., a strictly perpendicular shock. Previous works were focused on the impact of shock nonstationarity along the shock normal (self-reformation along x-axis) due to the accumulation of reflected ions over a foot distance from the ramp [*Yang et al.*, 2009a, 2011a]. Mixing together all nonstationarity effects along the shock normal and along the shock front is left for further work, but previously requires a better understanding of the shock front activity which is under active investigation. All the processes responsible for the front ripples under consideration in the present study are intrinsic to the shock dynamics itself; these do not require any external input process. In contrast, we also know that the upstream solar wind may include pre-existing large-scale turbulence [*Guo and Giacalone*, 2010], so waves activity of different scales may compete with each other and have some impact on ion acceleration. This can be also the case of an Alfvén wave interacting with a collisionless shock front [*Lu et al.*, 2009]. Such topics will be also analyzed in further works.

[72] **Acknowledgments.** This work has been performed while one of the authors (ZY) was staying in LATMOS (France) which is thanked for its hospitality and access to computing facilities. This research work was partly supported by the National Science Foundation of China (grant 40974083, 40974103, 41031064, 40890164, 40725013, 41104090, 41104091), Ocean public Welfare Scientific research Project, State Oceanic Administration of People's Republic of China (201005017), the Youth Fund of Polar Research Institute of China (CX20120101), Chinese Academy of Sciences KJCX2-YW-N28 and the Foundation of the Strategic Study of Chinese Polar Expedition Development 201136. The initial two-dimensional PIC simulations have been performed on the supercomputer of IDRIS center located at Orsay (near Paris).

[73] Philippa Browning thanks the reviewers for their assistance in evaluating this paper.

References

Axford, W. I., E. Lee, and G. Skadron (1977), The acceleration of cosmic rays by shock waves, *Proc. Int. Conf. Cosmic Rays 15th*, *11*, 132.

Begelman, M., and J. G. Kirk (1990), Shock-drift particle acceleration in superluminal shocks: A model for hot spots in extragalactic radio sources, *Astrophys. J.*, *353*, 66.

Bell, A. R. (1978a), The acceleration of cosmic rays in shock front: I, *Mon. Not. R. Astrophys. Soc.*, *182*, 147.

Bell, A. R. (1978b), The acceleration of cosmic rays in shock front: II, *Mon. Not. R. Astrophys. Soc.*, *182*, 443.

Berezhko, E. G., and H. J. Völk (2000), Galactic gamma-ray background radiation from supernova remnants, *Astrophys. J.*, *540*, 923.

Biskamp, D., and H. Welter (1972), Ion heating in high-Mach-number, oblique, collisionless shock waves, *Phys. Rev. Lett.*, *28*, 410.

Blandford, R. D., and J. P. Ostriker (1978), Particle acceleration by astrophysical shocks, *Astrophys. J.*, *221*, L29.

Blandford, R. D., and D. Eichler (1987), Particle acceleration at astrophysical shocks: A theory of cosmic ray origin, *Phys. Rep.*, *154*, L1.

Burgess, D., W. P. Wilkinson, and S. J. Schwartz (1989), Ion distribution and thermalizaiton at perpendicular and quasi-perpendicular supercritical collisionless shocks, *J. Geophys. Res.*, *94*, 8783.

Chalov, S. V. (2001), Shock drift acceleration of pickup protons at corotating interaction regions, *J. Geophys. Res.*, *106*, 18,667.
Chapman, S. C., R. E. Lee, and R. O. Dendy (2005), Perpendicular shock reformation and ion acceleration, *Space Sci. Rev.*, *121*, 5.
Czechowski, A., H. Fichtner, S. Grzedzielski, M. Hilchenbach, K. C. Hsieh, J. R. Jokipii, T. Kausch, J. Kota, and A. Shaw (2001), Anomalous cosmic rays and the generation of energetic neutrals in the region beyond the termination shock, *Astron. Astrophys.*, *368*, 622.
Decker, R. B. (1988), Computer modeling of test particle acceleration at oblique shocks, *Space Sci. Rev.*, *48*, 195.
Decker, R. B. (1990), Particle acceleration at shocks with surface ripples, *J. Geophys. Res.*, *95*(A8), 11,993.
Decker, R. B., and L. Vlahos (1985), Shock drift acceleration in the presence of waves, *J. Geophys. Res.*, *90*, 47.
Ellison, D. C., and S. P. Reynolds (1991), Electron acceleration in a nonlinear shock model with applications to supernova remnants, *Astrophys. J.*, *382*, 242.
Ellison, D. C., F. C. Jones, and M. G. Baring (1999), Direct acceleration of pickup ions at the solar wind termination shock: The production of anomalous cosmic rays, *Astrophys. J.*, *512*, 403.
Forslund, D. W., K. B. Quest, J. U. Brackbill, and K. Lee (1984), Collisionless dissipation in quasi-perpendicular shocks, *J. Geophys. Res.*, *89*(A4), 2142.
Giacalone, J., and R. Decker (2010), The origin of low-energy anomalous cosmic rays at the solar-wind termination shock, *Astrophys. J.*, *710*, 91.
Guo, F., and J. Giacalone (2010), Effect of large-scale magnetic turbulence on the acceleration of electrons by perpendicular collisionless shocks, *Astrophys. J.*, *715*, 406.
Hada, T., M. Oonishi, B. Lembège, and P. Savoini (2003), Shock front nonstationarity of supercritical perpendicular shocks, *J. Geophys. Res.*, *108* (A6), 1233, doi:10.1029/2002JA009339.
Hellinger P., P. Travnicek, B. Lembège, and P. Savoini (2007), Emission of nonlinear whistler waves at the front of perpendicular supercritical shocks: Hybrid versus full particle simulations, *Geophys. Res. Lett.*, *34*, L14109, doi:10.1029/2007GL030239.
Hudson, P. D. (1965), Reflection of charged particles by plasma shocks, *Mon. Not. R. Astron. Soc.*, *131*, 23.
Katsouleas, T., and J. M. Dawson (1983), Unlimited electron acceleration in laser-driven plasma waves, *Phys. Rev. Lett.*, *51*, 392.
Knuth, D. E. (1981), *The Art of Computer Programming: Semi Numerical Algorithms*, vol. 2, 2nd ed., Addison-Wesley, Reading, Mass.
Krymsky, G. F. (1977), A regular mechanism for accelerating charged particles at the shock front, *Dokl. Akad. Nauk SSSR*, *234*, 1306.
Lee, M. A. (1983), Coupled hydromagnetic wave excitation and ion acceleration at interplanetary travling shocks, *J. Geophys. Res.*, *88*(A8), 6109.
Lee, M. A. (1999), The injection, acceleration, and dynamical influence of interstellar pickup ions at the solar wind termination shock, *Astrophys. Space Sci.*, *264*, 497.
Lee, M. A., V. D. Shapiro, and R. Z. Sagdeev (1996), Pickup ion energization by shock surfing, *J. Geophys. Res.*, *101*, 4777.
Lee, R. E., S. C. Chapman, and R. O. Dendy (2005), Ion acceleration processes at reforming collisionless shocks, *Phys. Plasma*, *12*, 012901.
Lembège, B., and J. M. Dawson (1987), Self-consistent study of a perpendicular collisionless and nonresistive shock, *Phys. Fluids.*, *30*, 1767.
Lembège, B., and P. Savoini (1992), Nonstationarity of a two-dimensional quasiperpendicular supercritical collisionless shock by self-reformation, *Phys. Fluids B*, *4*, 3533.
Lembège, B., P. Savoini, P. Hellinger, and P. Travnicek (2009), Nonstationarity of a two-dimensional perpendicular shock: Competing mechanisms, *J. Geophys. Res.*, *114*, A03217, doi:10.1029/2008JA013618.
Lever, E. L., K. B. Quest, and V. D. Shapiro (2001), Shock surfing vs. shock drift acceleration, *Geophys. Res. Lett.*, *28*, 1367.
Lowe, R. E., and D. Burgess (2003), The properties and causes of rippling in quasi-perpendicular collisionless shock fronts, *Ann. Geophys.*, *21*, 671.
Lu, Q. M., Q. Hu, and G. P. Zank (2009), The interaction of Alfvén waves with perpendicular shocks, *Astrophys. J.*, *706*, 687.
Matsukiyo, S., M. Scholer, and D. Burgess (2007), Pickup protons at quasi-perpendicular shocks: Full particle electrodynamic simulations, *Ann. Geophys.*, *25*, 283.
Mazelle, C., B. Lembège, A. Morgenthaler, K. Meziane, T. S. Horbury, V. Genot, E. A. Lucek, and I. Dandouras (2010), Self-reformation of the quasi-perpendicular shock: Cluster observations, in *Twelfth International Solar Wind Conference*, edited by M. Maksimovic et al., *AIP Conf. Proc.*, *1216*, 471, doi:10.1063/1.3395905.
Meyer, J.-P., L. O. Drury, and D. C. Ellison (1998), A cosmic-ray composition controlled by volatility and A/Q ratio. SNR shock acceleration of gas and dust, *Space Sci. Rev.*, *86*, 179.
Mikić, Z., and M. A. Lee (2006), An introduction to shock and models of CMEs, shock and solar energetic particles, *Space Sci. Rev.*, *123*, 57, doi:10.1007/s11214-006-9012-2.
Moullard, O., D. Burgess, T. S. Horbury, and E. A. Lucek (2006), Ripples observed on the surface of the Earth's quasi-perpendicular bow shock, *J. Geophys. Res.*, *111*, A09113, doi:10.1029/2005JA011594.
Morse, D. L., W. W. Destler, and P. L. Auer (1972), Nonstationary behavior of collisionless shocks, *Phys. Rev. Lett.*, *28*, 13.
Nishimura, K., H. Matsumoto, H. Kojima, and S. P. Gary (2003), Particle simulation of re-formation at collisionless perpendicular shocks: Coherent behavior of reflected ions, *J. Geophys. Res.*, *108*(A5), 1182, doi: 10.1029/2002JA009671.
Reames, D. V. (2000), Particle acceleration by CME-driven shock waves, in *26th International Cosmic Ray Conference*, edited by B. L. Dingus, D. B. Kieda, and M. H. Salamon, *AIP Conf. Proc.*, *516*, 289.
Sagdeev, R. Z. (1966), Cooperative phenomena and shock waves in collisionless plasmas, *Rev. Plasma Phys.*, *4*, 23.
Saito, S., and T. Umeda (2011), suppression of reflected electrons by kinetic Alfvén turbulence in a quasi-perpendicular shock: Particle-in-cell simulations, *Astrophys. J.*, *736*, 35.
Scholer, M., and S. Matsukiyo (2004), Nonstationarity of quasi-perpendicular shocks: A comparison of full particle simulations with different ion to electron mass ratio, *Ann. Geophys.*, *22*, 2345.
Scholer, M., I. Shinohara, and S. Matsukiyo (2003), Quasi-perpendicular shocks: Length scale of the cross-shock potential shock reformation, and implication for shock surfing, *J. Geophys. Res.*, *108*(A1), 1014, doi: 10.1029/2002JA009515.
Shapiro, V. D., and D. Üçer (2003), Shock surfing acceleration, *Planet Space Sci.*, *51*, 665.
Walker, S. N., and M. A. Balikhin (1999), Ramp nonstationarity and the generation of whistler waves upstream of a strong quasiperpendicular shock, *Geophys. Res. Lett.*, *26*(10), 1357.
Webb, G. M., W. I. Axford, and T. Terasawa (1983), On the drift mechanism for energetic charged particles at shocks, *Astrophys. J.*, *270*, 537.
Webb, G. M., G. P. Zank, M. Ko, and D. J. Donohue (1995), Multidimensional Green's functions and the statistics of diffusive shock acceleration, *Astrophys. J.*, *453*, 178.
Winske, D., and K. B. Quest (1988), Magnetic field and density fluctuations at perpendicular supercritical collisionless shocks, *J. Geophys. Res.*, *93* (A9), 9681.
Yang, Z. W., Q. M. Lu, B. Lembège, and S. Wang (2009a), Shock front nonstationarity and ion acceleration in supercritical perpendicular shocks, *J. Geophys. Res.*, *114*, A03111, doi:10.1029/2008JA013785.
Yang, Z. W., Q. M. Lu, and S. Wang (2009b), The evolution of the eletric field at a nonstationary perpendicular shock, *Phys. Plasmas*, *16*, 1.
Yang, Z. W., B. Lembège, and Q. M. Lu (2011a), Impact of the nonstationarity of a supercritical perpendicular collisionless shock on the dynamics and energy spectra of pickup ions, *J. Geophys. Res.*, *116*, A08216, doi:10.1029/2010JA016360.
Yang, Z. W., B. Lembège, and Q. M. Lu (2011b), Acceleration of heavy ions by perpendicular collisionless shocks: Impact of the shock front non-stationarity, *J. Geophys. Res.*, *116*, A10202, doi:10.1029/2011JA016605.
Zank, G. P., H. L. Pauls, I. H. Cairns, and G. M. Webb (1996), Interstellar pickup ions and quasi-perpendicular shocks: Implications for the termination shock and interplanetary shocks, *J. Geophys. Res.*, *101*, 457.
Zank, G. P., G. Li, V. Florinski, Q. Hu, D. Lario, and C. W. Smith (2006), Particle acceleration at perpendicular shock waves: Model and observations, *J. Geophys. Res.*, *111*, A06108, doi:10.1029/2005JA011524.